Temperature-dependent chemical shift in the aqueous solution of xenon

Master's Thesis

Petri Peuravaara
NMR Research Unit
University of Oulu

2017

Contents

Chapter 1

Introduction

In nuclear magnetic resonance (NMR) spectroscopy, ^{129}Xe is commonly used as a probe to investigate different materials since its shielding constant is very sensitive to its environment [1–5]. The property of particular interest in the present work is the temperature dependence of the xenon chemical shift in an aqueous solution of xenon. At standard pressure, the xenon chemical shift is found to have a maximum at 315.3 K and 311.1 K for D_2O and H_2O solutions, respectively, while the well-known temperature of maximum density occurs at 284.34 K for D_2O and at 277.13 K for H_2O [6]. The theoretical background behind the existence of the chemical shift maximum as well as the peculiar offset found in its temperature is studied in this work.

The fact that NMR properties are very sensitive to the chemical environment makes their precise theoretical evaluation from first principles very difficult. In the case of an atom in a solution, the nuclear shielding is heavily influenced by the dynamics of the surrounding solvent, which are in turn dictated by both the temperature and the potential surface. This work approaches this problem by means of a molecular dynamics (MD) simulation. In an MD simulation, the classical equations of motion are solved numerically for the molecular system of interest to calculate the trajectories of the atoms. Extracting momentary geometries at certain time intervals, calculating the nuclear shielding for them with quantum-chemical (QC) methods and then averaging over them has been one of the more successful ways of recreating the gas-to-liquid shifts of water when compared to, for instance, continuum models that treat the solvent as a surrounding dielectric medium [7]. Unfortunately, this kind of approach leaves little room for interpreting the result in terms of well-defined structural and dynamic properties of the system. Therefore, a semianalytical model, in which the water around the xenon atom is interpreted to form a shell of uniform density, was also used to see if there could be found a qualitative way to explain the phenomenon.

The MD simulation used in this work was performed using the AMOEBA (atomic multipole optimized energetics for biomolecular applications) polarisable force field [8], which has the benefit of being able to reproduce the existence of the temperature of the density maximum of liquid water. However, the fact that the simulated maximum occurs at 290 K [9] suggests that the temperature-dependent data extracted from the simulation trajectory must be considered accurate in the qualitative sense only. The water-water interactions of the AMOEBA force field were used as such in the simulation, but the Xe – H_2O potential was customised by fitting to first-principles calculations of the Xe – H_2O dimer.

In the second chapter, a description of the basic principles behind both the molec-

ular dynamics simulation and the quantum-chemical methods used in the present work is provided. Also, the AMOEBA force field is described in detail. Even though a lot of the material in the molecular dynamics section overlaps the content of my bachelor's thesis [10], some of the information is repeated in the present work for the sake of completeness. The third chapter gives more specific details on how the MD simulation and the QC computations were carried out in the system of intrigue. Also, the semianalytical cavity model for the xenon chemical shift is introduced and explained. Finally, in the fourth chapter, the results of the described methods are reported and discussed.

Chapter 2

Theory

2.1 Molecular dynamics

2.1.1 General theory

This section uses the book *Understanding Molecular Simulation: From Algorithms to Applications* by Frenkel and Smit [11] as a general reference.

Newton equation of motion with many atoms

Molecular dynamics simulation is used to solve the many-body problem that arises, for instance, when modeling a liquid in which the macroscopic properties are due to a huge number of interacting particles. Because of this, solving the Newton equations of motion is not possible to do analytically, which calls for the use of numerical methods.

Let the simulation consist of N atoms and let the position of particle i be represented by vector $\boldsymbol{r}_i$. According to Newton's second law, for every particle i at time t

$$m_i \frac{\mathrm{d}^2 \boldsymbol{r}_i(t)}{\mathrm{d}t^2} = \boldsymbol{F}_i(t), \tag{2.1}$$

where m_i the mass of atom i and $\boldsymbol{F}_i = -\nabla U_i$, where U_i is the potential energy of the particle, is the force acting upon it. Using the Taylor series expansion, for a small time interval Δt, the position at time $t + \Delta t$ will become

$$\boldsymbol{r}_i(t + \Delta t) = \boldsymbol{r}_i(t) + \frac{\mathrm{d}\boldsymbol{r}_i(t)}{\mathrm{d}t}\Delta t + \frac{1}{2}\frac{\mathrm{d}^2 \boldsymbol{r}_i(t)}{\mathrm{d}t^2}\Delta t^2 + \frac{1}{6}\frac{\mathrm{d}^3 \boldsymbol{r}_i(t)}{\mathrm{d}t^3}\Delta t^3 + \cdots \tag{2.2}$$

and, accordingly, at time $t - \Delta t$,

$$\boldsymbol{r}_i(t - \Delta t) = \boldsymbol{r}_i(t) - \frac{\mathrm{d}\boldsymbol{r}_i(t)}{\mathrm{d}t}\Delta t + \frac{1}{2}\frac{\mathrm{d}^2 \boldsymbol{r}_i(t)}{\mathrm{d}t^2}\Delta t^2 - \frac{1}{6}\frac{\mathrm{d}^3 \boldsymbol{r}_i(t)}{\mathrm{d}t^3}\Delta t^3 + \cdots, \tag{2.3}$$

which will result via Eq. (2.1) in

$$\boldsymbol{r}_i(t + \Delta t) \approx 2\boldsymbol{r}_i(t) - \boldsymbol{r}_i(t - \Delta t) + \frac{\boldsymbol{F}_i(t)}{m_i}\Delta t^2, \tag{2.4}$$

the so-called Verlet integration method, which is one of the most widely used integration schemes for MD. The method also serves as a starting point for many more complicated integration algorithms.

As an MD simulation uses a finite Δt, it is an inevitable fact that, sooner or later, the predicted trajectories of the molecules will differ radically from the real ones. However, the purpose of an MD simulation is not to actually predict the exact trajectories but to produce statistical information about the system in question. Therefore, when choosing Δt, it's enough to make it small compared to the correlation times of the quantities relevant to the simulation, such as the total energy of the system [12]. Usually Δt is chosen to be somewhere around a femtosecond in atomistic simulations.

The integration algorithm used in the present work is the Beeman integration method [13], which is a predictor-corrector method. In these kind of methods, the integration consists of two parts. Firstly, the predictor part, where the distances $\boldsymbol{r}_i$, their derivatives and some of their higher derivatives (the acceleration at least) are estimated at time the $t + \Delta t$ in a similar manner as described above. After that the forces acting on the particles are calculated at the new coordinates, which leads to the acceleration through Eq. (2.1). Naturally, this gives a result different from the one acquired in the predictor part. The corrector part of the integration uses the difference between the two accelerations

$$\Delta \boldsymbol{r}_i^{(2)} = \boldsymbol{r}_{i,\text{corrected}}^{(2)} - \boldsymbol{r}_{i,\text{predicted}}^{(2)} \tag{2.5}$$

in order to estimate a correction to the predicted positions and their derivatives. The superscript (n) denotes the nth derivative of the position. The corrected values are

$$\boldsymbol{r}_{i,\text{corrected}}^{(n)} = \boldsymbol{r}_{i,\text{predicted}}^{(n)} + w_n \Delta \boldsymbol{r}_i^{(2)}, \tag{2.6}$$

where the weights w_n depend on the algorithm in use. They are usually chosen as a compromise between the accuracy, speed and stability of the method, stability in this case meaning, for instance, the ability to conserve the total energy of the system. For the Beeman algorithm, the predictor part produces trajectories identical with the Verlet integration method but the velocities are computed more accurately. Correctors exist only for the coordinates and velocities, not for any higher order derivatives.

Periodic boundary conditions

In an MD simulation the number of atoms is typically $10 \leq N \leq 100000$, which is little compared to the actual number. This is problematic because when using, *e.g.*, a cubic simulation box, a significant portion of the molecules lie near the boundaries of the box, which is not a desired setup when studying, for example, a bulk liquid. A widely used solution to this conundrum is the use of so-called periodic boundary conditions. In this approach the simulation box is considered a unit cell for a periodic lattice spanning all directions, illustrated in Fig. 2.1.

Molecular dynamics in constant temperature and pressure

The easiest kind of MD simulation to consider is one of constant total energy and volume, for the laws of motion keep the total energy of the system constant, at least within the accuracy of the integration and force evaluation algorithms. When considering a system in a constant temperature, however, the contact with the thermal bath must be implemented somehow. One deterministic way of doing so is the use of the Nosé-Hoover thermostat [14, 15]. The thermostat extends the Hamiltonian of the system with a new variable s so that it becomes

$$\mathcal{H}_{\text{Nosé}} = \sum_{i=1}^{N} \frac{p_i^2}{2m_i} + U(\{\boldsymbol{r}_i\}) + \frac{\xi^2 Q}{2} + 3N \frac{\ln s}{\beta}, \tag{2.7}$$

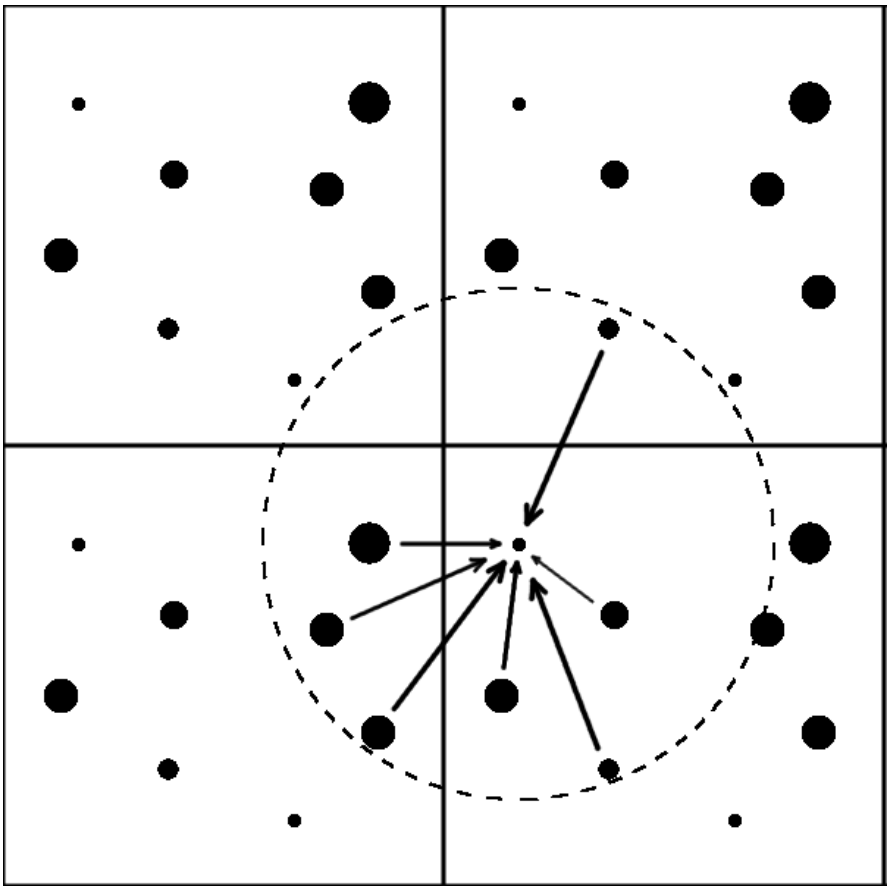

Figure 2.1: Visualisation of the periodic boundary conditions. The figure conforms to the minimum image convention, *i.e.*, the distance between the particles is taken to be the shortest among the possible periodic images. The forces acting on a certain atom are depicted with arrows. The dashed circle represents the cutoff distance of the atom.

where $\xi = sp_s/Q$, $\beta = 1/k_BT$ and Q is a fictional mass associated with s. It can be shown that, with this kind of inclusion, all the expectation values of quantities that depend only on the atomic positions or momenta will follow the canonical distribution. This distribution will come about regardless of the choice of Q but its magnitude will determine how quickly the system will react to fluctuations in temperature. A small Q, for example, corresponds to small inertia of the heat bath and will cause a swift response to a change in temperature.

In order to implement a coupling to a pressure bath, the side length of the simulation box must be interpreted as a dynamic variable. The Berendsen barostat [16, 17], which was used in the present work, carries this out by scaling the coordinates and the box length with respect to the center at every time step by a factor

$$\mu = \left[1 - \frac{\kappa \Delta t}{\tau_P}(P_0 - P)\right]^{1/3}, \tag{2.8}$$

where κ is the compressibility of the substance at constant temperature, P is the momentary pressure, P_0 is the desired constant pressure and τ_P is a time constant depicting the strength of the coupling.

Multipole expansion

The typical way of treating the electric field induced by an atom in MD is the multipole expansion. The potential V of a charge distribution localized around $\boldsymbol{r}$ can be expressed as a sum[1]

$$V(\boldsymbol{r}) = \frac{1}{4\pi\varepsilon_0} \sum_{n=0}^{\infty} \frac{1}{r^{n+1}} \int (r')^n P_n(\cos\theta')\rho(\boldsymbol{r}')\,\mathrm{d}\boldsymbol{r}', \tag{2.9}$$

where θ' is the angle between vectors $\boldsymbol{r}$ and $\boldsymbol{r}'$, ρ is the charge density function and P_n is a Legendre polynomial[2] of order n [18]. The first term integral in the expansion

$$q = \int \rho(\boldsymbol{r}')\,\mathrm{d}\boldsymbol{r}' \tag{2.10}$$

is clearly the total charge. The integral in the second term can be written in the form

$$\int r' \cos\theta' \rho(\boldsymbol{r}')\,\mathrm{d}\boldsymbol{r}' = \frac{1}{r}\int \boldsymbol{r}\cdot\boldsymbol{r}'\rho(\boldsymbol{r}')\,\mathrm{d}\boldsymbol{r}' = \frac{\boldsymbol{r}\cdot\boldsymbol{\mu}}{r}, \tag{2.11}$$

where

$$\boldsymbol{\mu} = \int \boldsymbol{r}'\rho(\boldsymbol{r}')\,\mathrm{d}\boldsymbol{r}' \tag{2.12}$$

is the dipole moment. The third integral is

$$\int (r')^2 \frac{1}{2}(3\cos^2\theta' - 1)\rho(\boldsymbol{r}')\,\mathrm{d}\boldsymbol{r}' = \frac{\boldsymbol{r}^T\boldsymbol{Q}\boldsymbol{r}}{2r^2}, \tag{2.13}$$

where $\boldsymbol{Q}$ is the quadrupole moment tensor, defined as

$$Q_{ij} = \int [3r_i'r_j' - (r')^2\delta_{ij}]\rho(\boldsymbol{r}')\,\mathrm{d}\boldsymbol{r}'. \tag{2.14}$$

Similar procedure can be continued and the fourth term would involve an octupole moment, for example. The more localized the charge distribution is, the swifter the sum (2.9) converges. When it comes to MD, the quadrupole moment is usually as far as one needs to go.

Even if all of the static multipoles of an atom are zero, as is the case with noble gas atoms, the electric field caused by the permanent multipoles in other atoms will distort its otherwise isotropic charge distribution. Typically, only the dipole moment needs to be considered for the purposes of MD. In the first-order approximation, the induced dipole moment for atom i is

$$\boldsymbol{\mu}_i^{\mathrm{ind}} = \alpha_i \boldsymbol{\mathcal{E}}_i \tag{2.15}$$

where α_i is its static dipolar polarisability and $\boldsymbol{\mathcal{E}}_i$ is the electric field around the atom. Polarisability is a tensor in general, but it can be replaced with a single number in the case of initially isotropic charge distribution. This approach serves as a practical approximation in the case of molecules, as well. Polarisability volume is defined as $\alpha_i/4\pi\varepsilon_0$ and the term is used interchangeably with polarisability in this work [19].

[1] $\int \ldots \mathrm{d}\boldsymbol{r}$ denotes a three-dimensional integration over all space.
[2] $P_0(x) = 1$, $P_1(x) = x$, $P_2(x) = \frac{1}{2}(3x^2 - 1)$, etc.

Analysing the simulation trajectory

An MD simulation will produce a series of instantaneous molecular geometries that, as such, provide little information about the statistical properties of the system. Special methods must therefore be used to analyze the resulting trajectory. For simple structural properties, the radial distribution function (RDF) $g(r)$ is a very informative property. It depicts the probability of finding two particles at a distance r from each other with respect to a uniformly random distribution, namely the ideal gas distribution.[3] In an MD simulation, the RDF can be defined more elaborately as

$$g(r) = \lim_{\mathrm{d}r \to 0} \frac{N_{\mathrm{d}r}(r)}{4\pi(N_{\mathrm{pairs}}/V)r^2\,\mathrm{d}r}, \tag{2.16}$$

where V is the volume of the simulation box and N_{pairs} is the number of possible unique combinations of the two atoms to which the RDF is being calculated [20]. $N_{\mathrm{d}r}$ is the average number of pairs whose distances from one another is between r and $r + \mathrm{d}r$ and it can be evaluated quite straightforwardly from the the geometries.

Another useful quality is the coordination number Z, which, for a liquid, is defined as the average number of atoms within the first solvation shell of the atom. The radius of the first solvation shell is defined as the distance to the first minimum of the RDF.

2.1.2 Interactions in the AMOEBA force field

Ref. [21] was used as a source in this section.

AMOEBA is a polarisable force field, *i.e.*, a force field which calculates the electric field resulting from polarisation explicitly at each time step. The potential energy U is expressed as a sum

$$U = U_{\mathrm{bond}} + U_{\mathrm{angle}} + U_{\mathrm{b}\theta} + U_{\mathrm{oop}} + U_{\mathrm{torsion}} + U_{\mathrm{vdW}} + U_{\mathrm{ele}}^{\mathrm{perm}} + U_{\mathrm{ele}}^{\mathrm{ind}}, \tag{2.17}$$

where the terms U_{bond}, U_{angle}, $U_{\mathrm{b}\theta}$, U_{oop} and U_{torsion} depict intramolecular valence interactions. U_{vdW}, $U_{\mathrm{ele}}^{\mathrm{perm}}$ and $U_{\mathrm{ele}}^{\mathrm{ind}}$ are the nonbonded contributions and they are the only terms relevant for intermolecular interactions. The short-range valence interactions are empirical functions of bond lengths and bond angles and they were left untouched in the parameterisation of the present work.

Nonbonded interactions in the AMOEBA force field consist of the van der Waals potential U_{vdW} as well as the electrostatic potential due to, on the one hand, permanent multipoles ($U_{\mathrm{ele}}^{\mathrm{perm}}$) and, on the other hand, induced multipoles ($U_{\mathrm{ele}}^{\mathrm{ind}}$). The van der Waals potential of AMOEBA between two atoms i and j is written in the form

$$U_{\mathrm{vdW}}(r_{ij}) = \varepsilon_{ij} \left(\frac{1.07}{\rho_{ij} + 0.07} \right)^7 \left(\frac{1.12}{\rho_{ij}^7 + 0.12} - 2 \right), \tag{2.18}$$

where

$$\rho_{ij} = r_{ij}/R_{ij}^0, \tag{2.19}$$

r_{ij} being the distance between the atoms,

$$\varepsilon_{ij} = \frac{4\varepsilon_{ii}\varepsilon_{jj}}{(\varepsilon_{ii}^{1/2} + \varepsilon_{jj}^{1/2})^2} \tag{2.20}$$

[3] For a uniformly random distribution, $g(r) \equiv 1$.

and

$$R_{ij}^0 = \frac{(R_{ii}^0)^3 + (R_{jj}^0)^3}{(R_{ii}^0)^2 + (R_{jj}^0)^2}. \tag{2.21}$$

R_{ii}^0 and ε_{ii} are the distance and interaction strength parameters specific to atoms of type i. R_{ii}^0 represents the distance in which the potential reaches its minimum and ε_{ii} is the depth of the said minimum. Permanent multipoles up to quadrupoles reside at each atomic center and constitute a multipole vector for atom i as

$$\boldsymbol{M}_i^T = [q_i, \mu_{ix}, \mu_{iy}, \mu_{iz}, Q_{ixx}, Q_{ixy}, Q_{ixz}, ..., Q_{izz}], \tag{2.22}$$

where q_i is the charge of atom i, $\boldsymbol{\mu}_i$ its dipole moment and $\boldsymbol{Q}_i$ is its quadrupole moment tensor. With the multipole vector, the energy of the interaction for atom i and j is

$$U_{\text{elec}}^{\text{perm}}(r_{ij}) = \boldsymbol{M}_i^T \boldsymbol{T}_{ij} \boldsymbol{M}_j \tag{2.23}$$

where[4]

$$T_{ij} = \begin{pmatrix} 1 & \frac{\partial}{\partial x_j} & \frac{\partial}{\partial y_j} & \frac{\partial}{\partial z_j} & \cdots \\ \frac{\partial}{\partial x_i} & \frac{\partial^2}{\partial x_i \partial x_j} & \frac{\partial^2}{\partial x_i \partial y_j} & \frac{\partial^2}{\partial x_i \partial z_j} & \cdots \\ \frac{\partial}{\partial y_i} & \frac{\partial^2}{\partial y_i \partial x_j} & \frac{\partial^2}{\partial y_i \partial y_j} & \frac{\partial^2}{\partial y_i \partial z_j} & \cdots \\ \frac{\partial}{\partial z_i} & \frac{\partial^2}{\partial z_i \partial x_j} & \frac{\partial^2}{\partial z_i \partial y_j} & \frac{\partial^2}{\partial z_i \partial z_j} & \cdots \\ \vdots & \vdots & \vdots & \vdots & \ddots \end{pmatrix} \left(\frac{1}{r_{ji}}\right). \tag{2.24}$$

Polarisation is treated via induced dipoles at the atomic centers. The induced dipole moment is defined as in Eq. (2.15) where $\boldsymbol{\mathcal{E}}_i$ is the electric field produced by both all the static multipoles in the atoms of other molecules and the induced dipoles in all of the atoms, including the ones in the same molecule. However, the electric field $\boldsymbol{\mathcal{E}}_i$ depends on the said dipoles as well, which means that Eq. (2.15) must be solved iteratively.

When r_{ij} is small enough, it becomes unphysical to represent the charge distribution of the atom with multipoles in a single point. This causes the polarisation energy to diverge at this limit, which is problematic when treating intramolecular polarisation. A damping mechanism introduced by Thole [22] was used to avoid this so-called "polarisation catastrophe". In this mechanism one of the two point charges, it doesn't matter which [22], in each pairwise interaction of induced dipoles is replaced by a charge distribution, which in AMOEBA has the form

$$\rho = \frac{3a}{4\pi} \exp(-au^3), \tag{2.25}$$

where $u = R_{ij}/(\alpha_i \alpha_j)^{1/6}$ and a is the dimensionless Thole factor. Because of this, the elements of the matrix T_{ij} are in these situations modified by a factor which depends on the interaction type, given by Thole [22] for the point charge, and Ren *et al.* [8] for the higher multipoles.

2.2 General quantum chemistry

The purpose of this section is to introduce the numerical methods that are used in the present work to solve the Schrödinger equation for a system of molecules. Unless noted otherwise, this section uses the book *Molecular Quantum Mechanics* by Atkins and Friedman as a reference [19].

[4] The factor $1/4\pi\varepsilon_0$ is omitted.

2.2.1 Born-Oppenheimer approximation

In general, the Schrödinger equation cannot be solved analytically, which calls for the use of approximations. One of the most fundamental of these is the Born-Oppenheimer approximation. The nuclei are very slow compared to the electrons due to their mass difference, which makes it plausible to solve the Schrödinger equation for the electrons alone, keeping the nuclei at set positions. The energy acquired by the Schrödinger equation in this case will naturally depend on the coordinates of the nuclei, which determines the potential energy surface of the system.

The equation to solve becomes

$$\hat{H}\Psi(\boldsymbol{r};\boldsymbol{R}) = E(\boldsymbol{R})\Psi(\boldsymbol{r};\boldsymbol{R}), \tag{2.26}$$

$$\hat{H} = -\frac{\hbar^2}{2m_e}\sum_{i=1}^{N_e}\nabla_i^2 - j_0\sum_{i=1}^{N_e}\sum_{I=1}^{N_n}\frac{Z_I}{r_{Ii}} + \frac{1}{2}j_0\sum_{i\neq j}^{N_e}\frac{1}{r_{ij}}, \tag{2.27}$$

where $\Psi(\boldsymbol{r};\boldsymbol{R})$ is the wave function when the electron coordinates $\boldsymbol{r}$ are the variables and the nuclei coordinates $\boldsymbol{R}$ are fixed. $E(\boldsymbol{R})$ is the energy corresponding to this configuration, $j_0 = e^2/4\pi\varepsilon_0$, N_e and N_n are the total numbers of electrons and nuclei, correspondingly, Z_I is the atomic number of nucleus I, r_{Ii} is the distance between nucleus I and electron i and r_{ij} is the distance between electrons i and j. When solving for the energy and many other properties of a system consisting of multiple atoms from quantum mechanics alone, as opposed to using experiments as a reference, usually the challenge lies in solving this equation with sufficient accuracy.

2.2.2 Hartree-Fock

Hartree-Fock (HF) method approximates the many-electron wave function Ψ with a single Slater determinant

$$\Psi(1,2,\ldots,N_e) = \left(\frac{1}{N_e!}\right)^{1/2}\begin{vmatrix} \phi_1(1) & \phi_2(1) & \cdots & \phi_{N_e}(1) \\ \phi_1(2) & \phi_2(2) & \cdots & \phi_{N_e}(2) \\ \vdots & \vdots & \ddots & \vdots \\ \phi_1(N_e) & \phi_2(N_e) & \cdots & \phi_{N_e}(N_e) \end{vmatrix}. \tag{2.28}$$

The idea is to find spinorbitals $\phi_1, \phi_2, \ldots$ [5] that produce the minimum energy for the wave function. Implementing some variational calculus, one can derive the so-called Hartree-Fock equations[6] for the molecular orbitals ψ_m

$$\hat{f}_1\psi_m(1) = \varepsilon_m\psi_m(1), \tag{2.29}$$

where

$$\hat{f}_1 = \hat{h}_1 + \sum_{m'}[2\hat{J}_{m'}(1) - \hat{K}_{m'}(1)] \tag{2.30}$$

$$\hat{J}_{m'}(1)\psi_m(1) = j_0\left[\int \psi_{m'}^*(2)\frac{1}{r_{12}}\psi_{m'}(2)\,\mathrm{d}\tau_2\right]\psi_m(1) \tag{2.31}$$

[5] Spinorbitals are the product of the molecular orbital ψ_m and the spin wave function in the case of weak spin-orbit coupling.

[6] This form of the equations is only applicable to a closed-shell system.

$$\hat{K}_{m'}(1)\psi_m(1) = j_0 \left[\int \psi^*_{m'}(2) \frac{1}{r_{12}} \psi_m(2)\, \mathrm{d}\tau_2 \right] \psi_{m'}(1) \tag{2.32}$$

$$\hat{h}_1 = -\frac{\hbar^2}{2m_e}\nabla_1^2 - j_0 \sum_I^{N_n} \frac{Z_I}{r_{I1}}. \tag{2.33}$$

Here, ψ_m are the molecular orbitals, $\hat{f}_1$ is the Fock-operator, $\hat{J}_m$ is the Coulomb operator, $\hat{K}_m$ is the exchange operator, and $\hat{h}_1$ is the one-electron Hamiltonian[7] and ε_m the orbital energy.

The optimal ψ_m can be found through iteration and for atoms, the results are the atomic orbitals. When applying the HF procedure in a system of multiple atoms, however, the numerical solution is most of the time too complicated. This calls for the use of a new approach. If the molecular orbitals are depicted as linear combinations of atomic orbitals (LCAO)

$$\psi_m = \sum_{o=1}^{N_o} c_{om}\chi_o, \tag{2.34}$$

where the χ_o are the atomic orbitals used as basis functions and N_o their total number, then one can derive the so-called Roothaan equations:

$$\sum_{o=1}^{N_o} F_{o'o}c_{om} = \varepsilon_m \sum_{o=1}^{N_o} S_{o'o}c_{om}, \tag{2.35}$$

where

$$S_{o'o} = \int \chi^*_{o'}(1)\chi_o(1)\, \mathrm{d}\tau_1 \tag{2.36}$$

and

$$F_{o'o} = \int \chi^*_{o'}(1) f_1 \chi_o(1)\, \mathrm{d}\tau_1. \tag{2.37}$$

Through iteration, one can find the coefficients c_{om} that produce the minimum energy. At the limit of an infinite basis, this energy is called the Hartree-Fock limit.

2.2.3 Post-Hartree-Fock methods

Eqs. (2.31) and (2.32) show that the molecular orbitals produced by Hartree-Fock experience the other electrons only through the averaged change in potential energy that they cause. Because of this, the instantaneous interactions of the electrons remain ignored. The inclusion of this so-called electron correlation is the improvement that post-Hartree-Fock (pHF) methods focus on. The difference between the HF energy and the real energy is called correlation energy.

The following pHF methods, *i.e.*, the Møller-Plesset perturbation theory (MPBT) and the coupled-cluster (CC) method, are so-called size-consistent in the limit of infinite separation and size-extensive in the limit of infinite number of electrons. The lack of these physical properties would cause an error that would increase with the size of the system, which is a problem in many other pHF methods.

[7] Hamiltonian for one electron in the presence of the nuclei only.

Møller-Plesset perturbation theory

The energy acquired by the HF method can be improved through perturbation theory. In the so-called Møller-Plesset perturbation theory the unperturbed Hamiltonian is

$$\hat{H}^{(0)} = \hat{H}_{\mathrm{HF}} = \sum_{i=1}^{N_e} \hat{f}_i, \tag{2.38}$$

which means that the perturbation is

$$\hat{H}^{(1)} = \hat{H} - \hat{H}_{\mathrm{HF}} = \frac{1}{2} j_0 \sum_{i \neq j} \frac{1}{r_{ij}} - \sum_{i,m} [2\hat{J}_m(i) - \hat{K}_m(i)]. \tag{2.39}$$

The HF energy E_{HF} is the expectation value of H with the unperturbed HF wave function so it's a sum of the zeroth and first order energies $E_0^{(0)}$ and $E_0^{(1)}$. The second-order correction is

$$E^{(2)} = \sum_{J \neq 0} \frac{\left\langle \Psi_0 | \hat{H}^{(1)} | \Psi_J \right\rangle \left\langle \Psi_J | \hat{H}^{(1)} | \Psi_0 \right\rangle}{E_0^{(0)} - E_J^{(0)}}, \tag{2.40}$$

and including it will result in the so-called MP2 energy. MP2 usually overestimates the effect of electron correlation. When calculating the potential energy surface, this will often cause the minimum to be too steep.

Coupled-cluster method

CC method uses the so-called cluster operator $\hat{C}$, which is related to the real wave function Ψ by

$$\Psi = e^{\hat{C}} \Psi_0, \tag{2.41}$$

where Ψ_0 is the HF wave function. Let $\hat{C}_1$ be an operator that, when operating on Ψ_0, forms a linear combination of single-excitation Slater determinants, *i.e.*,

$$\hat{C}_1 \Psi_0 = \sum_{a,p} t_a^p \Psi_a^p. \tag{2.42}$$

Accordingly, let $\hat{C}_2$ be the corresponding operator for double-excitation Slater determinants,

$$\hat{C}_2 \Psi_0 = \sum_{a,b,p,q} t_{ab}^{pq} \Psi_{ab}^{pq}, \tag{2.43}$$

all the way up to $\hat{C}_N$ where N is the total number of electrons. The coefficients t_a^p are called single-excitation amplitudes, t_{ab}^{pq}, correspondingly, double-excitation amplitudes and so on. The cluster operator can be written as a sum

$$\hat{C} = \hat{C}_1 + \hat{C}_2 + \cdots + \hat{C}_N. \tag{2.44}$$

When the expression for the cluster operator and Eq. (2.41) are substituted into the Schrödinger equation, the amplitudes $t_a^p, t_{ab}^{pq}, \ldots$ can be solved iteratively.

Because of computational demands, the sum in Eq. (2.44) is commonly truncated to include only the first two terms and this is referred to "coupled cluster with singles and doubles" (CCSD). If, in addition, $\hat{C}_3$ is included via perturbation theory, it's referred to as "coupled cluster with singles, doubles and perturbative triples" [CCSD(T)]. Like MPBT, CC is not a variational method in the sense that it will not result in a systematic upper limit for the energy of the system. The CC energy can often be seen to oscillate around the true energy as more of the excitations are taken into account.

2.2.4 Density functional theory

The idea behind density functional theory is to express the properties of the system using the electron probability density ρ. As proved by Hohenberg and Kohn [23], the electron density and the ground state energy E have one-to-one correspondence, which makes it possible to express the energy as a functional $E[\rho]$. It's conventional to write the functional as

$$E[\rho] = T[\rho] + V_{ee}[\rho] + \int \rho(\boldsymbol{r})\nu(\boldsymbol{r})\,\mathrm{d}\boldsymbol{r}, \tag{2.45}$$

where

$$\nu(\boldsymbol{r}) = -j_0 \sum_I^{N_n} \frac{Z_I}{|\boldsymbol{r} - \boldsymbol{r}_I|} \tag{2.46}$$

is the interaction energy between the nuclei and an electron at location $\boldsymbol{r}$ and it's called the external potential. The first term on the right-hand side of Eq. (2.45) corresponds to the kinetic energy and the second term is the electron-electron repulsion energy.

As DFT has only one three-dimensional function as opposed to a $3N_e$-dimensional wave function, with constraints guaranteeing antisymmetry, handling DFT computationally can be a lot more straightforward. The density must conserve the total number of electrons, *i.e.*,

$$N_e - \int \rho(\boldsymbol{r})\,\mathrm{d}\boldsymbol{r} = 0. \tag{2.47}$$

Hohenberg-Kohn variational theory

The fundamental equation for DFT is acquired via the Hohenberg-Kohn variational theorem [23], which states that, for a trial electron density $\rho'(\boldsymbol{r})$, the energy functional $E[\rho']$ cannot be lower than the true ground-state energy. This means that the variation of the true ground state energy functional must vanish:

$$\delta E[\rho] = 0. \tag{2.48}$$

However, this formulation does not account for the fact that the functional is subject to the constraint (2.47). This limitation can be tended by using the method of undetermined multipliers, in which the constraint (2.47) is varied and multiplied with μ, the so-called Lagrange multiplier, and then added to Eq. (2.48). Because the right-hand side of Eq. (2.47) is zero, this will not affect the right-hand side of Eq. (2.48), either, and will result in

$$\delta\left\{E[\rho] - \mu \int \rho(\boldsymbol{r})\,\mathrm{d}\boldsymbol{r}\right\} = 0. \tag{2.49}$$

Because the integral depends only on ρ and not any of its derivatives, the variation of the energy is simply

$$\delta E[\rho] = \int \frac{\delta E[\rho]}{\delta\rho(\boldsymbol{r})}\delta\rho(\boldsymbol{r})\,\mathrm{d}\boldsymbol{r} = \int \mu\,\delta\rho(\boldsymbol{r})\,\mathrm{d}\boldsymbol{r} \tag{2.50}$$

from which, by comparison, the expression for μ can be found:

$$\mu = \frac{\delta E[\rho]}{\delta\rho(\boldsymbol{r})} = \nu(\boldsymbol{r}) + \frac{\delta E_{\mathrm{HK}}[\rho]}{\delta\rho(\boldsymbol{r})} \tag{2.51}$$

where $E_{\mathrm{HK}}[\rho] = T[\rho] + V_{ee}[\rho]$.

Kohn-Sham equations

Let a reference system consist of N_e non-interacting electrons in an external potential $\nu_{\text{ref}}(\boldsymbol{r})$ such that its electron density $\rho_{\text{ref}}(\boldsymbol{r})$ is the same as the true electron density. The energy functional of the actual system can be written

$$E[\rho] = T_{\text{ref}}[\rho] + J[\rho] + \int \rho(\boldsymbol{r})\nu(\boldsymbol{r})\,\mathrm{d}\boldsymbol{r} + E_{\text{XC}}[\rho], \tag{2.52}$$

where

$$E_{\text{XC}}[\rho] = T[\rho] + V_{ee}[\rho] - (T_{\text{ref}}[\rho] + J[\rho]) \tag{2.53}$$

is the exchange-correlation energy. $J[\rho]$ is the classical Coulombic electron-electron potential energy

$$J[\rho] = \frac{j_0}{2}\int \frac{\rho(\boldsymbol{r}_1)\rho(\boldsymbol{r}_2)}{|\boldsymbol{r}_1 - \boldsymbol{r}_2|}\,\mathrm{d}\boldsymbol{r_1}\mathrm{d}\boldsymbol{r_2}. \tag{2.54}$$

If an effective potential ν_{eff} is defined

$$\nu_{\text{eff}}(\boldsymbol{r}) = \nu(\boldsymbol{r}) + \frac{\delta J[\rho]}{\delta\rho(\boldsymbol{r})} + \nu_{\text{XC}}, \tag{2.55}$$

where

$$\nu_{\text{XC}} = \frac{\delta E_{\text{XC}}[\rho]}{\delta\rho(\boldsymbol{r})} \tag{2.56}$$

then Eq. (2.51) becomes

$$\mu = \nu_{\text{eff}}(\boldsymbol{r}) + \frac{\delta T_{\text{ref}}[\rho]}{\delta\rho(\boldsymbol{r})}. \tag{2.57}$$

The expression for the variational derivative of the Coulombic potential energy can be found in a similar fashion as in Eq. (2.50), which gives

$$\frac{\delta J[\rho]}{\delta\rho(\boldsymbol{r})} = j_0\int \frac{\rho(\boldsymbol{r}_2)}{|\boldsymbol{r} - \boldsymbol{r}_2|}\,\mathrm{d}\boldsymbol{r}_2. \tag{2.58}$$

Because the electrons in the reference system are non-interacting, the equation for μ in the reference system would identical to one in Eq. (2.57) except that it would contain ν_{ref} instead of ν_{eff}. In other words, solving the electron density for a system of interacting electrons is equivalent to solving it for a system of non-interacting electrons in an effective external potential ν_{eff}. Again, because the electrons are non-interacting, solving the Schrödinger equation is straightforward. The exact ground-state wave function can be represented by a Slater determinant

$$\Psi = \left(\frac{1}{N_e!}\right)^{1/2}\begin{vmatrix} \phi_1^{\text{KS}}(1) & \phi_2^{\text{KS}}(1) & \cdots & \phi_{N_e}^{\text{KS}}(1) \\ \phi_1^{\text{KS}}(2) & \phi_2^{\text{KS}}(2) & \cdots & \phi_{N_e}^{\text{KS}}(2) \\ \vdots & \vdots & \ddots & \vdots \\ \phi_1^{\text{KS}}(N_e) & \phi_2^{\text{KS}}(N_e) & \cdots & \phi_{N_e}^{\text{KS}}(N_e) \end{vmatrix}, \tag{2.59}$$

where ϕ_m^{KS} are the Kohn-Sham spinorbitals, each of which is a product of the one-electron Kohn-Sham orbital ψ_m^{KS} and the corresponding spin state wave function. The orbitals are acquired by solving the so-called Kohn-Sham equation

$$\left\{\hat{h}_1 + j_0\int \frac{\rho(\boldsymbol{r}_2)}{|\boldsymbol{r}_1 - \boldsymbol{r}_2|}\,\mathrm{d}\boldsymbol{r}_2 + \nu_{\text{XC}}\right\}\psi_m^{\text{KS}}(\boldsymbol{r}_1) = \varepsilon_m^{\text{KS}}\psi_m^{\text{KS}}(\boldsymbol{r}_1), \tag{2.60}$$

where h_1 is, again, the one-electron Hamiltonian [24]. The electron density can be expressed in terms of the spinorbitals as

$$\rho(\boldsymbol{r}) = \sum_{i=1}^{N_e} \left|\phi_i^{\mathrm{KS}}(\boldsymbol{r})\right|^2 . \tag{2.61}$$

Local density approximation

The fundamental difficulty in DFT is determining the exchange-correlation energy functional E_{XC}. One of the simplest approaches to approximate it is the local density approximation (LDA) [25]. If the electron density was uniform, *i.e.*, the system under consideration was a homogeneous electron gas, the exchange-correlation energy could simply be written as

$$E_{\mathrm{XC}}[\rho] = \int \rho(\boldsymbol{r})\varepsilon_{\mathrm{XC}}(\rho(\boldsymbol{r}))\,\mathrm{d}\boldsymbol{r} \tag{2.62}$$

where $\varepsilon_{\mathrm{XC}}(\rho(\boldsymbol{r}))$ is the exchange-correlation energy per electron as a function of the uniform density. In this case Eq. (2.56) becomes

$$\nu_{\mathrm{XC}} = \rho(\boldsymbol{r})\frac{\mathrm{d}\varepsilon_{\mathrm{XC}}(\rho(\boldsymbol{r}))}{\mathrm{d}\rho(\boldsymbol{r})} + \varepsilon_{\mathrm{XC}}(\rho(\boldsymbol{r})). \tag{2.63}$$

In LDA, in every point $\boldsymbol{r}$ in space, ν_{XC} and $\varepsilon_{\mathrm{XC}}$ are taken to be the same as for the homogeneous electron gas. However, though $\rho(\boldsymbol{r})$ is taken to be constant in that point, this value will be different for each $\boldsymbol{r}$, hence the name "local density approximation". $\varepsilon_{\mathrm{XC}}$ is typically expressed as an analytical function of the electron density, parameterised via Monte Carlo simulations [26].

Generalised-gradient approximation

The exchange-correlation functional be further improved by using a more general form for the integrand in Eq. (2.62). As the name suggests, the generalised-gradient approximation (GGA) [27, 28] includes the gradient of the electron density in the functional, which has the form

$$E_{\mathrm{XC}}^{\mathrm{GGA}}[\rho] = \int f\left(\rho(\boldsymbol{r}), \nabla\rho(\boldsymbol{r})\right)\,\mathrm{d}\boldsymbol{r}. \tag{2.64}$$

The term f, like $\varepsilon_{\mathrm{XC}}$, is an analytical function, but more elaborate schemes are required to determine its exact form. One way to do it by comparison with the HF exchange-correlation energy.

Hybrid functionals

The main characteristic of the so-called hybrid functionals is that E_{XC} is treated as a linear combination of the exact HF exchange energy and DFT exchange and correlation functionals with varying coefficients. Using this kind of approach has been found to give more accurate values for, for instance, atomisation energies, bond lengths and vibrational frequencies of most molecules than the simpler functionals [29]. In the present study, Becke's "half-and-half" theory is used [30] with the Lee-Yang-Parr (LYP) correlation functional [31], abbreviated BHandHLYP. The form of the exchange-correlation functional is

$$E_{\mathrm{XC}} = 0.5 \cdot E_{\mathrm{X}}^{\mathrm{HF}} + 0.5 \cdot (E_{\mathrm{X}}^{\mathrm{LDA}} + \Delta E_{\mathrm{X}}^{\mathrm{B88}}) + E_{\mathrm{C}}^{\mathrm{LYP}}, \tag{2.65}$$

where $E_{\mathrm{X}}^{\mathrm{HF}}$ is the HF exchange energy, $E_{\mathrm{X}}^{\mathrm{LDA}}$ is the LDA exchange energy, $\Delta E_{\mathrm{X}}^{\mathrm{B88}}$ is Becke's 1988 correction functional to the LDA energy [28] and $E_{\mathrm{C}}^{\mathrm{LYP}}$ is the LYP correlation energy.

2.2.5 Basis sets

In order to describe the wave function perfectly, an infinite number of basis functions χ_o are required. In practice, a finite number is always used and the choice will greatly affect, not only how accurate the calculation is, but also how demanding the calculation is computationally. For these reasons, the choice of the basis set is an important part of first-principles calculations.

Gaussian-type orbitals

Gaussian-type orbitals (GTO) are of the form

$$g_{ijk}(\boldsymbol{r}) = Nx^i y^j z^k e^{-\alpha r^2}, \tag{2.66}$$

where i, j and k are non-negative integers, N is the normalization constant and α is a positive exponent. GTOs do not represent the true form of the orbitals as well as Slater-type orbitals (STO) that are proportional to $e^{-\alpha r}$ instead of $e^{-\alpha r^2}$. However, GTOs are handy when computing systems with three or more atoms, for a product of two Gaussians with different centers is another Gaussian, whose center lies at a point between the centers of the two original Gaussians. This usually makes GTOs more cost-effective to evaluate.

The sum $l = i + j + k$ defines the angular momentum type for the function. $l = 1$ corresponds to a p-type function, for example. If l for the target atom is higher than necessitated by the elementary valence theory, the function is called a polarisation function. The inclusion of polarisation functions serves as a way of taking into account the distortion of the atomic orbitals due to the presence of other atoms.

Contracted basis sets

As mentioned above, GTOs do not portray the orbitals as faithfully as the STOs. This means that more GTOs are needed to reach the same precision. This problem can be alleviated by the use of contracted basis sets. The atomic orbitals are represented as linear combinations of the primitive GTOs in Eq. (2.66):

$$\chi_o = \sum_i d_{oi} g_i, \tag{2.67}$$

where the constants d_{oi} are the contraction coefficients. They are chosen in such a way that the new atomic orbitals describe the system better than the same number of primitive Gaussians, which will reduce the amount of unknowns c_{om} to solve.

Correlation consistent basis sets

The correlation consistent (cc)[8] basis sets are contracted basis sets that are designed to recover the correlation energy of the electrons [32]. The cc split-valence basis sets[9] are labeled according to their size with letter combinations (from small to large) cc-pVDZ,

[8] Abbreviated with lowercase letters in order to avoid confusion with the coupled-cluster method.

[9] For the valence electrons only as opposed to all-electron basis sets.

cc-pVTZ, cc-pVQZ, cc-pV5Z and cc-pV6Z (correlation consistent polarised Valence Double/Triple/Quadruple/Quintuple/Sextuple Zeta). A step up in quality means the addition of one new exponent to each basis function type as well as the addition of a new type of polarisation function. The inclusion of extra diffuse functions is noted by attaching the prefix "aug-" to the acronym (*e.g.*, aug-cc-pVDZ), which means adding one function with a smaller exponent for each angular momentum type. Since the diffuse functions extend far from the nucleus, they are of importance for long-range interactions.

The benefit from using cc basis sets is the possibility for basis-set extrapolation for they are geared for systematic approach towards the limit of an infinite basis set. This makes it possible to estimate the said limit, even if the calculations were carried out with only two or three (aug)-cc-pVnZ -type basis sets [32].

Basis-set superposition error

The potential energy between two molecules is calculated

$$V_{\text{dim}} = E_{\text{dim}} - E_1 - E_2, \tag{2.68}$$

where E_{dim} is the total energy of the dimer and E_1 and E_2 are the energies of the separate molecules. This is an example of a situation when the so-called basis-set superposition error becomes significant and requires treatment. If, in the calculations of the single molecular energies, the basis set is defined only for that molecule, there will an error due to the fact that the basis is smaller than for the dimer. This error can be treated with counterpoise correction, *i.e.*, by including the basis functions of the other molecule as well in the calculation of the separate molecules.

2.3 Determination of NMR properties

In this section, the theory behind the determination of NMR parameters via electronic wave function, as well as some computational aspects behind it, are discussed [7].

2.3.1 Nuclear spin Hamiltonian

The effective nuclear spin Hamiltonian for an NMR experiment can in general be written as[10]

$$\hat{H} = -\sum_I \gamma_I \hbar \boldsymbol{B}^T (\mathbf{1} - \boldsymbol{\sigma}_I) \hat{\boldsymbol{I}}_I + \frac{1}{2} \sum_{I \neq J} \gamma_I \gamma_J \hbar^2 \hat{\boldsymbol{I}}_I^T (\boldsymbol{D}_{IJ} + \boldsymbol{K}_{IJ}) \hat{\boldsymbol{I}}_J, \tag{2.69}$$

where $\boldsymbol{B}$ is the external magnetic field and γ_I, $\hat{\boldsymbol{I}}_I$ and $\boldsymbol{\sigma}_I$ are the magnetogyric ratio, the nuclear spin operator and the shielding tensor for nucleus I, respectively.[11] The magnetic moment of a nucleus can be written as

$$\boldsymbol{M}_I = \gamma_I \hbar \hat{\boldsymbol{I}}_I. \tag{2.70}$$

$\boldsymbol{D}_{IJ}$ is the direct dipolar coupling tensor and $\boldsymbol{K}_{IJ}$ is the reduced indirect spin-spin coupling tensor. In rapidly rotating molecules, the rotational averaging makes the contribution

[10] Superscript T denotes a transpose, $\mathbf{1}$ is the 3×3 identity matrix.

[11] For nuclei whose spin is more than 1/2, the Hamiltonian also contains term corresponding to quadrupole coupling, which has been omitted in Eq. (2.69).

from the direct dipolar coupling vanish entirely, and both the shielding tensor and the indirect spin-spin coupling tensor can be replaced with scalar quantities

$$\sigma_I = \frac{1}{3}\mathrm{Tr}\,\boldsymbol{\sigma}_I, \quad K_{IJ} = \frac{1}{3}\mathrm{Tr}\,\boldsymbol{K}_{IJ}, \tag{2.71}$$

the nuclear shielding constant and the reduced nuclear spin-spin coupling constant, respectively. The chemical shift δ is defined by means of the shielding constant and in the present work the form

$$\delta_I = \frac{\sigma_{\mathrm{ref}} - \sigma_I}{1 - \sigma_{\mathrm{ref}}} \tag{2.72}$$

is used. Here σ_{ref} is usually the shielding of nucleus I in an appointed system of reference. In the present study, the free xenon atom was used.

The fact that the magnitude of the NMR interactions is very small, allows interpreting them as perturbations to the electronic energy. The electronic energy can be expanded around zero magnetic field and zero magnetic moments, to the second order, as

$$E(\boldsymbol{B},\boldsymbol{M}) = E_0 + \frac{1}{2}\boldsymbol{B}^T\boldsymbol{E}^{(20)}\boldsymbol{B} + \sum_I \boldsymbol{B}^T\boldsymbol{E}_I^{(11)}\boldsymbol{M}_I + \frac{1}{2}\sum_{I\neq J}\boldsymbol{M}_I^T\boldsymbol{E}_{IJ}^{(02)}\boldsymbol{M}_J, \tag{2.73}$$

where the derivatives of the energy are denoted with tensors

$$\boldsymbol{E}^{(20)} = \left.\frac{\mathrm{d}^2E(\boldsymbol{B},\boldsymbol{M})}{\mathrm{d}\boldsymbol{B}^2}\right|_{\boldsymbol{B}=\boldsymbol{0},\boldsymbol{M}=\boldsymbol{0}} \tag{2.74}$$

$$\boldsymbol{E}_I^{(11)} = \left.\frac{\mathrm{d}^2E(\boldsymbol{B},\boldsymbol{M})}{\mathrm{d}\boldsymbol{B}\,\mathrm{d}\boldsymbol{M}_I}\right|_{\boldsymbol{B}=\boldsymbol{0},\boldsymbol{M}=\boldsymbol{0}} \tag{2.75}$$

$$\boldsymbol{E}_{IJ}^{(02)} = \left.\frac{\mathrm{d}^2E(\boldsymbol{B},\boldsymbol{M})}{\mathrm{d}\boldsymbol{M}_I\,\mathrm{d}\boldsymbol{M}_J}\right|_{\boldsymbol{B}=\boldsymbol{0},\boldsymbol{M}=\boldsymbol{0}}, \tag{2.76}$$

where the notation

$$\frac{\mathrm{d}^2f}{\mathrm{d}\boldsymbol{u}\,\mathrm{d}\boldsymbol{v}} = \begin{pmatrix} \frac{\mathrm{d}^2f}{\mathrm{d}u_x\,\mathrm{d}v_x} & \frac{\mathrm{d}^2f}{\mathrm{d}u_x\,\mathrm{d}v_y} & \frac{\mathrm{d}^2f}{\mathrm{d}u_x\,\mathrm{d}v_z} \\ \frac{\mathrm{d}^2f}{\mathrm{d}u_y\,\mathrm{d}v_x} & \frac{\mathrm{d}^2f}{\mathrm{d}u_y\,\mathrm{d}v_y} & \frac{\mathrm{d}^2f}{\mathrm{d}u_y\,\mathrm{d}v_z} \\ \frac{\mathrm{d}^2f}{\mathrm{d}u_z\,\mathrm{d}v_x} & \frac{\mathrm{d}^2f}{\mathrm{d}u_z\,\mathrm{d}v_y} & \frac{\mathrm{d}^2f}{\mathrm{d}u_z\,\mathrm{d}v_z} \end{pmatrix} \tag{2.77}$$

is used. In Eqs. (2.74-2.76), all of the magnetic moments are denoted collectively as $\boldsymbol{M}$. The equation contains no first-order terms since they disappear in closed-shell systems. By comparing with Eq. (2.69), it can be seen that

$$\boldsymbol{\sigma}_I = \boldsymbol{E}_I^{(11)} + \boldsymbol{1} \tag{2.78}$$

$$\boldsymbol{K}_{IJ} = \boldsymbol{E}_{IJ}^{(02)} - \boldsymbol{D}_{IJ}, \tag{2.79}$$

i.e., the evaluation of the shielding constant and the coupling constant can be reduced to discussing the energy derivatives related to the electronic wave function.

2.3.2 Ramsey's expression for the nuclear shielding

The nonrelativistic Hamiltonian in the presence of an external magnetic field can be written as[12]

$$\begin{aligned}\hat{H}(\boldsymbol{B},\boldsymbol{M}) = \frac{1}{2}\sum_i \pi_i^2 - \sum_i \boldsymbol{m}_i \cdot \boldsymbol{B}^{\mathrm{tot}}(\boldsymbol{r}_i) - \sum_{iI}\frac{Z_I}{r_{iI}} + \frac{1}{2}\sum_{i\neq j}\frac{1}{r_{ij}} \\ + \frac{1}{2}\sum_{I\neq J}\frac{Z_I Z_J}{R_{IJ}} - \sum_I \boldsymbol{M}_I \cdot \boldsymbol{B}^{\mathrm{tot}}(\boldsymbol{R}_I) + \sum_{I>J}\boldsymbol{M}_I^T \boldsymbol{D}_{IJ}\boldsymbol{M}_J,\end{aligned} \tag{2.80}$$

where $\boldsymbol{m}_i$ are the spin magnetic moments of the electrons and

$$\boldsymbol{\pi}_i = -i\nabla_i + \boldsymbol{A}^{\mathrm{tot}}(\boldsymbol{r}_i) \tag{2.81}$$

is the kinetic momentum operator combined with the vector potential $\boldsymbol{A}^{\mathrm{tot}}$ of the magnetic field. The vector potential $\boldsymbol{A}'$ for a general magnetic field $\boldsymbol{B}'$ is defined only by the requirement of satisfying

$$\nabla \times \boldsymbol{A}' = \boldsymbol{B}'. \tag{2.82}$$

The superscripts "tot" in the magnetic field and the vector potential denote the fact that they consist of not only the external magnetic field $\boldsymbol{B}$ but also the contribution arising from the magnetic moments of the nuclei, *i.e.*,

$$\boldsymbol{A}^{\mathrm{tot}} = \boldsymbol{A}_O + \sum_I \boldsymbol{A}_I \tag{2.83}$$

$$\boldsymbol{B}^{\mathrm{tot}} = \boldsymbol{B} + \sum_I \boldsymbol{B}_I, \tag{2.84}$$

where subscripts I denote the individual nuclei. $\boldsymbol{A}_O$ is the vector potential for the homogeneous external field $\boldsymbol{B}$ and it can be expressed as

$$\boldsymbol{A}_O = \frac{1}{2}\boldsymbol{B} \times (\boldsymbol{r} - \boldsymbol{O}), \tag{2.85}$$

where $\boldsymbol{O}$ denotes the so-called gauge origin, a point in space that can be arbitrarily chosen when defining the vector potential of the field. Though the choice of the gauge origin does not matter when using an exact wave function, in approximate wave functions gauge invariance may become an issue, which is discussed more in section 2.3.4. The vector potential for the nuclei can be written as

$$\boldsymbol{A}_I(\boldsymbol{r}_i) = \alpha^2 \frac{\boldsymbol{M}_I \times \boldsymbol{r}_{iI}}{r_{iI}^3}, \tag{2.86}$$

where α is the fine-structure constant. Using the approach discussed above, the so-called Ramsey's expressions can be derived for the shielding tensor and the indirect spin-spin coupling tensor by expressing the energy derivatives with respect to the Hamiltonian using the second-order time-independent perturbation theory. For shielding, the expression is

$$\boldsymbol{\sigma}_I = \left\langle 0 \middle| \hat{\boldsymbol{h}}_{BI}^{\mathrm{dia}} \middle| 0 \right\rangle - 2\sum_{n_S\neq 0} \frac{\left\langle 0 \middle| \hat{\boldsymbol{h}}_B^{\mathrm{oz}} \middle| n_S \right\rangle \left\langle n_S \middle| (\hat{\boldsymbol{h}}_I^{\mathrm{pso}})^T \middle| 0 \right\rangle}{E_{n_S} - E_0}, \tag{2.87}$$

[12] In atomic units.

where

$$\hat{\boldsymbol{h}}_{BI}^{\mathrm{dia}} = \frac{\alpha^2}{2} \sum_i \frac{(\boldsymbol{r}_{iO} \cdot \boldsymbol{r}_{iI})\mathbf{1} - \boldsymbol{r}_{iI}\boldsymbol{r}_{iO}^T}{r_{iI}^3} \tag{2.88}$$

$$\hat{\boldsymbol{h}}_{B}^{\mathrm{oz}} = \frac{1}{2} \sum_i \hat{\boldsymbol{\ell}}_{iO} \tag{2.89}$$

$$\hat{\boldsymbol{h}}_{I}^{\mathrm{pso}} = \alpha^2 \sum_i \frac{\hat{\boldsymbol{\ell}}_{iI}}{r_{iI}^3}. \tag{2.90}$$

Operator $\hat{\boldsymbol{\ell}}_{iI}$ is the angular momentum operator for electron i, *i.e.*,

$$\hat{\boldsymbol{\ell}}_{iI} = -i\boldsymbol{r}_{iI} \times \nabla_i, \tag{2.91}$$

and $|n_S\rangle$ describes a singlet state.

The terms on the right-hand side of Eq. (2.87) are the diamagnetic part and the paramagnetic part, respectively. Typically, the diamagnetic part is dominant and results in a positive shielding constant in most cases and it corresponds to the expectation value of the unperturbed ground state. The paramagnetic part consists of a summation over all the singlet states and it is specified by the orbital motion of the electrons.

2.3.3 Variational perturbation theory

Though Ramsey's expression provides qualitative interpretation for the origin of the shielding, it is not very practical from a computational perspective since it requires information about the excited singlet states. Eq. (2.78) states that the shielding can be treated as a second-order derivative of the ground-state energy, which gives an opportunity to treat the problem using the so-called variational perturbation theory.

The electronic energy E can be denoted $E(\boldsymbol{B}, \boldsymbol{M}; \lambda)$ in which the parameter λ describes all the parameters other than $\boldsymbol{B}$ or $\boldsymbol{M}$ that contribute to it. The ground-state energy can be expressed as

$$E(\boldsymbol{B}, \boldsymbol{M}) = E(\boldsymbol{B}, \boldsymbol{M}; \lambda^*), \tag{2.92}$$

where λ^* corresponds to a set of parameters in which the energy is at its minimum. The variational principle states that

$$\left.\frac{\partial E(\boldsymbol{B}, \boldsymbol{M}; \lambda)}{\partial \lambda}\right|_{\lambda=\lambda^*} = 0 \tag{2.93}$$

for an arbitrary $\boldsymbol{B}$ and $\boldsymbol{M}$. When the derivative $E^{(11)}$ is evaluated while keeping this in mind, the expression for the nuclear shielding can be found to be

$$\boldsymbol{\sigma}_I = \mathbf{1} + \left[\frac{\partial^2 E(\boldsymbol{B}, \boldsymbol{M}; \lambda)}{\partial \boldsymbol{B} \partial \boldsymbol{M}_I} + \frac{\partial^2 E(\boldsymbol{B}, \boldsymbol{M}; \lambda)}{\partial \boldsymbol{M}_I \partial \lambda} \frac{\partial \lambda}{\partial \boldsymbol{B}}\right]\Bigg|_{\lambda=\lambda^*, \boldsymbol{B}=\mathbf{0}, \boldsymbol{M}=\mathbf{0}}, \tag{2.94}$$

if the differentiation with respect to the magnetic moment is performed first. The first term inside the brackets corresponds to the explicit second-order dependence of the electronic energy on $\boldsymbol{M}_K$ and $\boldsymbol{B}$ and it can be determined straightforwardly from the Hamiltonian. The second term contains also implicit dependence on the magnetic field $\boldsymbol{B}$, *i.e.*, the

dependence that arises due to the change in the wave function as the magnetic field varies. The derivative $\partial\lambda/\partial\boldsymbol{B}$ is the first-order response of the wave function with respect to the external magnetic field. Determining the shielding is straightforward after the response has been evaluated. Even though this method requires a fully variational wave function, this procedure can be implemented, with slight modifications, in the nonvariational case as well.

It's worth noting that an expression for the shielding can be also derived by differentiating first with respect to $\boldsymbol{B}$ and then with $\boldsymbol{M}_K$. However, this will result in responses of the form $\partial\lambda/\partial\boldsymbol{M}_K$, *i.e.*, the responses would have to be evaluated for each nucleus separately. This is why the expression in Eq. (2.94) is more common.

2.3.4 Gauge invariance

The choice of the gauge origin $\boldsymbol{O}$ in the expression for the vector potential of the external magnetic field in Eq. (2.85) does not have any effect on any observable property of the system. This physical requirement of gauge invariance is necessarily fulfilled by exact wave functions. With approximate wave functions, however, the gauge invariance is impossible to implement exactly. If the system consists of only one atom, the natural gauge origin is the atomic center for, as it turns out, the wave function is correct to the first order in the magnetic field $\boldsymbol{B}$ in that case. The same effect can be accomplished in molecules for a general gauge origin $\boldsymbol{O}$ by introducing a phase factor to the atomic orbitals χ_o, which will be transformed to

$$\omega_o(\boldsymbol{r}) = \exp\left(-\frac{1}{2}i[\boldsymbol{B}\times(\boldsymbol{R}_I-\boldsymbol{O})]\cdot\boldsymbol{r}\right)\chi_o(\boldsymbol{r}), \tag{2.95}$$

where $\boldsymbol{R}_I$ is the location of the nucleus. The benefit of this form is that it can be used for systems of multiple atoms, as well. The resulting atomic orbitals are called gauge-including atomic orbitals (GIAO) [33, 34].

2.4 Relativistic effects

So far, the energy and the nuclear shielding have been discussed only nonrelativistically (NR). Due to the heaviness of the xenon atom, the core electrons can have very high velocities, which means that relativity has to be treated somehow for accurate results. Here, a brief summary of the relativistic methods used in this study is provided, namely the effective core potential (ECP) and the zeroth-order regular approximation (ZORA) [32].

2.4.1 Effective core potential

Because the fully relativistic treatment requiring all-electron calculations is not computationally very efficient, reducing the calculation back to the NR level would be convenient. The effective core potential (ECP)[13] approach makes use of the fact that the relativistic effects concern mostly the core electrons and replaces a certain number of them with an effective potential. The so-called norm-conserving potentials are fitted so that the solution of the Schrödinger equation produces the same valence orbitals as the fully relativistic calculation.[14] The so-called energy-consistent potentials, on the other hand, are adjusted

[13] Also called pseudopotential (PP).

[14] Technically, pseudo-orbitals formed by removing the nodal structure of the real orbitals near the core.

to the total energies of the system. The ECP used for the xenon in the present work, ECP28MDF [35], is of the latter type. The ECP approach is reliable for calculating the potential energy surface of xenon with water, since only the valence electrons are important for the interaction. However, it cannot be relied on when calculating, for instance, the heavy-atom nuclear shielding, which depends also on the core electrons themselves. Furthermore, the ECP approach can account only for the scalar-relativistic (SR) part of the relativistic effects, not the spin-orbit (SO) part.

2.4.2 Zeroth-order regular approximation

In relativistic quantum mechanics, the time-independent Schrödinger equation is replaced by its relativistic counterpart, the time-independent Dirac equation

$$\hat{H}_D \Psi_D = E \Psi_D, \tag{2.96}$$

where, in atomic units,

$$\hat{H}_D = c\boldsymbol{\alpha} \cdot \hat{\boldsymbol{p}} + \boldsymbol{\beta} c^2 + V \tag{2.97}$$

and β, as well as the components of vector $\boldsymbol{\alpha}$ ($\boldsymbol{\alpha}_x$, $\boldsymbol{\alpha}_y$ and $\boldsymbol{\alpha}_z$) are 4×4 matrices, $\hat{\boldsymbol{p}}$ is the linear momentum operator and V is potential energy. $\boldsymbol{\alpha}$ and $\boldsymbol{\beta}$ can be written in terms of 2×2 Pauli spin matrices and identity matrices as

$$\boldsymbol{\alpha}_{x,y,z} = \begin{pmatrix} \mathbf{0} & \boldsymbol{\sigma}_{x,y,z} \\ \boldsymbol{\sigma}_{x,y,z} & \mathbf{0} \end{pmatrix}; \qquad \beta = \begin{pmatrix} \mathbf{1} & \mathbf{0} \\ \mathbf{0} & \mathbf{-1} \end{pmatrix}. \tag{2.98}$$

The wave function Ψ_D has four components and can be written as

$$\Psi_D = \begin{bmatrix} \Psi_{L\alpha} \\ \Psi_{L\beta} \\ \Psi_{S\alpha} \\ \Psi_{S\beta} \end{bmatrix}, \tag{2.99}$$

where L and S refer to the so-called large and small components of the wave function, respectively, and α and β refer to the spin. Writing the $\boldsymbol{\alpha}$ and $\boldsymbol{\beta}$ matrices explicitly and shifting the zero of the energy by mc^2 ($m = 1$) allows splitting the equation into

$$c(\boldsymbol{\sigma}_s \cdot \hat{\boldsymbol{p}})\Psi_S + V\Psi_L = E\Psi_L \tag{2.100}$$

$$c(\boldsymbol{\sigma}_s \cdot \hat{\boldsymbol{p}})\Psi_L + (-2c^2 + V)\Psi_S = E\Psi_S, \tag{2.101}$$

where the spin matrices are denoted collectively $\boldsymbol{\sigma}_s = (\boldsymbol{\sigma}_x, \boldsymbol{\sigma}_y, \boldsymbol{\sigma}_z)$ and Ψ_L and Ψ_S are two-component functions

$$\Psi_L = \begin{pmatrix} \Psi_{L\alpha} \\ \Psi_{L\beta} \end{pmatrix} \qquad \Psi_S = \begin{pmatrix} \Psi_{S\alpha} \\ \Psi_{S\beta} \end{pmatrix}. \tag{2.102}$$

This will lead to equations

$$\left[c^2(\boldsymbol{\sigma}_s \cdot \hat{\boldsymbol{p}})(2c^2 - V)^{-1} K (\boldsymbol{\sigma}_s \cdot \hat{\boldsymbol{p}}) + V\right] \Psi_L = E\Psi_L \tag{2.103}$$

$$\Psi_S = K \frac{\boldsymbol{\sigma}_s \cdot \hat{\boldsymbol{p}}}{2c} \Psi_L, \tag{2.104}$$

where

$$K = \left(1 - \frac{V - E}{2c^2}\right)^{-1} = \frac{2c^2}{2c^2 - V}\left(1 + \frac{E}{2c^2 - V}\right)^{-1}. \tag{2.105}$$

The nonrelativistic limit ($c \to \infty$) leads to the Schrödinger equation. In the zeroth-order regular approximation (ZORA) method, the relativistic corrections are obtained by approximating $\left(1 + \frac{E}{2c^2 - V}\right) \approx 1$ in Eq. (2.105), which results in [36]

$$\left[V + \frac{1}{2}\mathcal{K}\hat{p}^2 + \frac{1}{2}\hat{\boldsymbol{p}} \cdot ([\hat{\boldsymbol{p}}\mathcal{K}] \times \hat{\boldsymbol{p}})\right] \Psi_L = E\Psi_L, \tag{2.106}$$

where

$$\mathcal{K} = \frac{1}{1 - V/2c^2}. \tag{2.107}$$

Omitting the last term on the left-hand side of Eq. (2.106), the spin-orbit (SO) interaction, results in the scalar-relativistic ZORA (SR-ZORA) approach, whereas its inclusion is referred to as the SO-ZORA method.

The approximation $E/(2c^2 - V) \approx 0$ is justified in regions where V is small when compared to E. Therefore, ZORA is a good approximation for valence orbitals and outer core orbitals, even for heavy atoms [36]. However, for a very large E, such as the innermost electrons in very heavy atoms, the error is substantial. Moreover, it is not invariant with respect to energy scale, which can be seen by the term of V instead of $(V - E)$ in the expression for $\mathcal{K}$.

Chapter 3

Calculations

3.1 First-principles calculation of the xenon-water potential energy

Xe–H_2O interactions in the AMOEBA force field were parameterised with *ab initio* potential surface calculations for the dimer at the HF, MP2, CCSD and CCSD(T) levels of theory with Molpro quantum chemistry package [37–40]. For xenon, ECP was used, replacing 28 innermost electrons (ECP28MDF by Peterson *et al.* [35]). The energies of the dimer were computed with five different water molecule orientations, depicted in Fig. 3.1. The calculations were carried out with Xe–O distances 3.4 Å to 5.6 Å with the interval of 0.2 Å and 5.6 Å to 8.0 Å with the interval of 0.4 Å. The water molecules were in all cases in the AMOEBA equilibrium geometry, *i.e.*, the O–H bond length was 0.9572 Å and the H–O–H bond angle was 108.5°. The basis sets for oxygen and hydrogen were of the aug-cc-pVnZ type [41]. Pseudopotential valence-only basis sets of type aug-cc-pVnZ-PP [35] were used for xenon. Counterpoise correction was used in all the calculations.

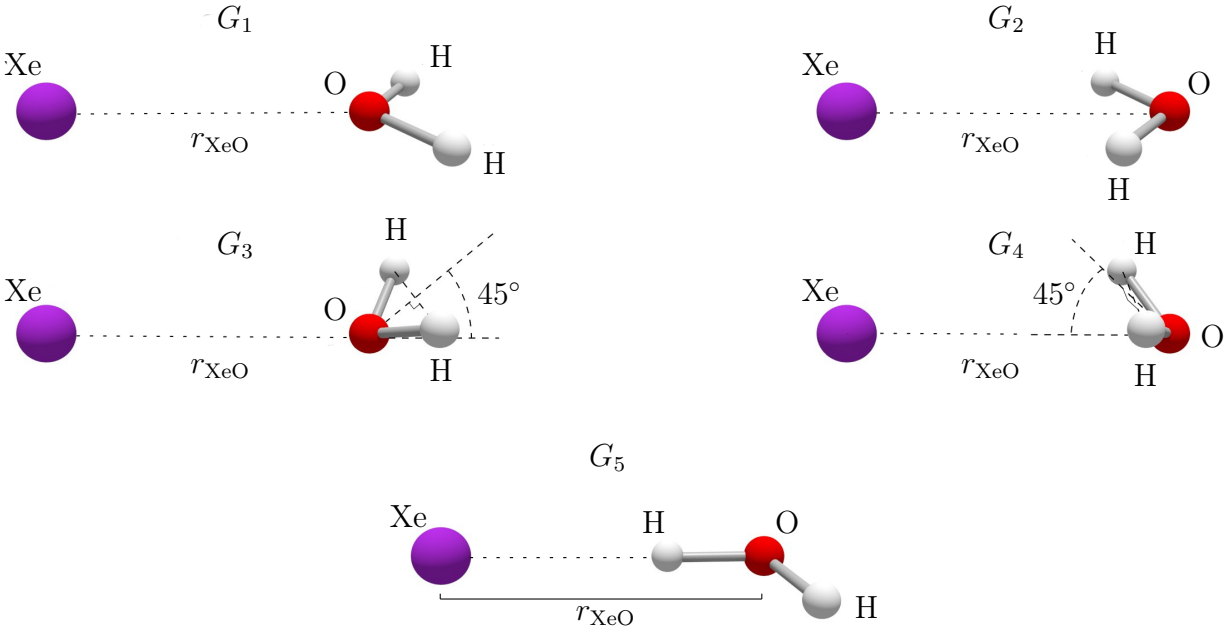

Figure 3.1: Orientations of the water molecule with respect to the xenon atom in the potential energy calculations of the Xe–H_2O dimer. In G_1, G_2 and G_5, all atoms are coplanar. In G_3 and G_4, the water dipole vector is tilted 45°.

First, the basis sets aug-cc-pVDZ(-PP) were used and the energies were calculated with the HF and MP2 levels of theory. After that, they were carried out with at the CCSD level with the same basis sets. The basis sets were then systematically improved up to aug-cc-pv5Z(-PP). In addition, a basis set expansion center was added halfway between the xenon and the oxygen. The exponents for the primitive basis functions located at the center were chosen to be 0.9, 0.3 and 0.1 for the s and p orbitals, 0.6 and 0.2 for the d and f orbitals and 0.35 for the g orbital [42, 43]. In the final CCSD calculation, the basis sets for oxygen and hydrogen were set to aug-cc-pV6Z. For xenon, the largest basis set available was the aug-cc-pV5Z. Therefore, additional diffuse primitive basis functions were added to s-, p-, d-, f-, g- and h-shells. The first exponent was chosen to be one third of the most diffuse exponent for that angular momentum type in the basis set, the second a third of that and so on. Finally, the calculation was repeated at the CCSD(T) level with these basis sets.

It's worth noting here that the static polarisability volume of 4.000 Å^3 for the xenon atom was also computed at the same level of theory (CCSD(T), ECP and aug-cc-pV5Z-PP basis) with the Gaussian software [44]. However, because the value acquired was only used in the force field parameterisation schemes that were not used in the actual production simulation, the computational aspects are not discussed further. Polarisability can nevertheless be acquired as a derivative of the total energy, in a manner similar to the case of nuclear shielding.

3.2 Parameterisation of the xenon-water pair potential

Xenon atom is neutral and spherical. Then, it can interact with water molecules only through the van der Waals interaction and the induction, parameterised by polarisability, in the AMOEBA force field. The corresponding force field parameters were least-squares fitted to the best interaction energy curve that was calculated from first principles. Five different parameterisation schemes were attempted:

1. The AMOEBA van der Waals parameters R_{ii} and ε were fitted for xenon.[1]

2. Both the van der Waals parameters and the xenon polarisability α_i were fitted.

3. In addition to the previous parameters, the Thole factor a was fitted for xenon as well.

4. The xenon-oxygen and the xenon-hydrogen van der Waals potential energies were expressed as

$$U_{\text{vdW}}(r_{ij}) = \sum_n \frac{C_n}{r_{ij}^n} \tag{3.1}$$

   instead of the AMOEBA characteristic form. The coefficients C_n were the fitted parameters and they were, naturally, different for Xe – H and Xe – O interactions. The xenon polarisability was maintained constant.

5. The xenon van der Waals potential was again of the form (3.1) and the polarisability and the Thole factor were fitted, as well.

[1] Eqs. (2.18)-(2.21).

The form of the potential in Eq. (3.1) was used only to be able to conveniently make a good fit to the QC data and the coefficients, therefore, bear no physical significance.

First, only the even integers were used in the sum (3.1), starting with $n = 6$. More terms were added until the fit would no longer improve, which was at $n = 12$. If the fit was not good enough at that point, also the odd values of n between 7 and 11 were included.

As mentioned in the previous section, the xenon polarisability volume of 4.000 Å^3 (experimental value acquired by Kumar and Meath being 4.025 Å^3 [45]) was used in the fitting schemes where the polarisability was not optimized. In schemes where the Thole factor was not optimized, the AMOEBA default value of $a = 0.390$ was used.

The van der Waals potential of the form (3.1) proved problematic due to the fact that the coefficients were not restrained in any way, which would cause the potential to wobble at large distances. As a bit rickety solution to this, different coefficients were used when the Xe – O or Xe – H distances were more than 4.8 Å. For the Xe – H potential, the best fit also had the problem of approaching minus infinity at small separation, which was fixed by using yet another function for distances smaller than 2.6 Å, using only exponents 6 and 12. In both of the fixes discussed, two of the coefficients were determined by the condition that the potential and its first derivative (and as a result, the forces on atoms) were continuous.[2]

The polarisability tended to ascend to values much larger than what is physically plausible in the fits 2, 3 and 5. In the fits 3 and 5, the Thole factor had this tendency as well. This was problematic since the induction energy iteration would not converge at small distances if either of these quantities were too high. Therefore, the maximum values for the xenon polarisability and Thole factor were restricted to 10.5 Å^3 and 0.6, respectively, as these values were the highest tested values that did not cause the simulation to crash. The fact that the physical interpretation for the polarisability parameter had, obviously, to be abandoned in order to reproduce the QC data, will be further discussed in section 4.1.

3.3 Molecular dynamics simulation

The MD simulations were performed using the Tinker molecular modeling package [8, 46] with one xenon atom and 255 water molecules. There were 10 simulations in total, each corresponding to one of the temperatures 278 K, 288 K, ..., 368 K. The parameters acquired by fit 5 of the previous section were used for the Xe – O and Xe – H interactions. The parameters for water-only interactions were adopted from the AMOEBA defaults. The Beeman integration algorithm [13] was used to calculate the molecular trajectories and the time step was 0.5 fs. The simulations were of the isothermal-isobaric type and the Berendsen barostat [16, 17] was used to accomplish the constant pressure of 1 atm with $\tau = 2.0$ ps, $\kappa = 0.000046$ bar^{-1}.[3] The simulation was first stabilised by running the simulation with the Bussi-Parrinello thermostat algorithm [47] for 18 ps. After that, the chained Nosé-Hoover by Martyna *et al.* [48] was used as the thermostat algorithm for the actual simulation for a duration of 3 ns. The Bussi-Parrinello algorithm was used for the stabilisation because it produced a stable temperature faster than the Nosé-Hoover algorithm.

[2] Both of the coefficients of the Xe – H potential at small distances were therefore determined by this condition.

[3] See section 2.1.1 for details of the parameters.

3.4 Computation of the nuclear shielding

The simulation trajectory was sampled for momentary configurations (snapshots) every 2125 steps (1.0625 ps). From these snapshots, geometries for $Xe(H_2O)_n$ clusters were extracted in such a way that the water molecules that were included had a hydrogen or oxygen within 5.5 Å from the xenon.[4] The nuclear shielding was calculated for these geometries with Turbomole [49] and Dalton [50] codes using the BHandHLYP hybrid density functional [30] with GIAOs with basis sets def-TZVP [51] for oxygen and hydrogen. For xenon, an uncontracted $(27s25p21d4f)$ basis set by Hanni [52], modified by Lantto to have four f-type functions instead of one [53], was used.[5]

Due to the computational cost, the calculation was nonrelativistic, which naturally produces an error in the shielding. Therefore, in order to estimate the magnitude of the error, the shielding calculation was also performed relativistically for selected two snapshots for each temperature. One of the snapshots was chosen completely randomly and the other was always the configuration of least energy among the extracted snapshots. The relativistic computation was carried out using the SO-ZORA approach [55–58] with the Amsterdam density functional (ADF) code [59, 60]. The shielding tensor calculation [61, 62] used finite Gaussian nuclear model [63]. The basis sets used Slater-type orbitals and they were all-electron jcpl for xenon and TZP for oxygen and hydrogen [64].

3.5 NMR force field

One way of determining the total xenon chemical shift in a general $Xe(H_2O)_n$ cluster is to approximate it as a sum of pairwise contribution from individual water molecules. This approach is also useful for the purposes of the semianalytical cavity model. For these reasons, a binary chemical shift function $\delta_{\text{pair}}(d)$ has to be defined.[6] Similarly as for the modified van der Waals potential in the MD simulation, the binary chemical shift function in the present work was expressed as

$$\delta_{\text{pair}}(d) = \sum_n \delta_n / d^n, \tag{3.2}$$

where the coefficients δ_n were acquired by fitting. The data to which the coefficients were fitted was determined in two distinct ways:

1. Pairwise-additive chemical shift (PCS) approach: the chemical shift was computed directly for Xe – H_2O dimers with the same nonrelativistic level of theory as for the MD snapshot clusters.

2. Effective pair chemical shift approach (EPCS): the chemical shift function was fitted by interpreting the QC chemical shift of the $Xe(H_2O)_n$ clusters[7] as a sum of pairwise contributions from each water molecule.

Obviously, to determine what kind of water molecule geometries to use in parameterising the cavity model, information is needed about the most probable water molecule

[4] Typically, the clusters contained 20 to 30 water molecules.

[5] The basis was originally developed for the purpose of determining the magnetic properties of ^{129}Xe in a van der Waals complex with a rubidium atom [54].

[6] d is the Xe–O distance.

[7] This comprised all of the truncated cluster snapshots that were used in the QC shielding calculation.

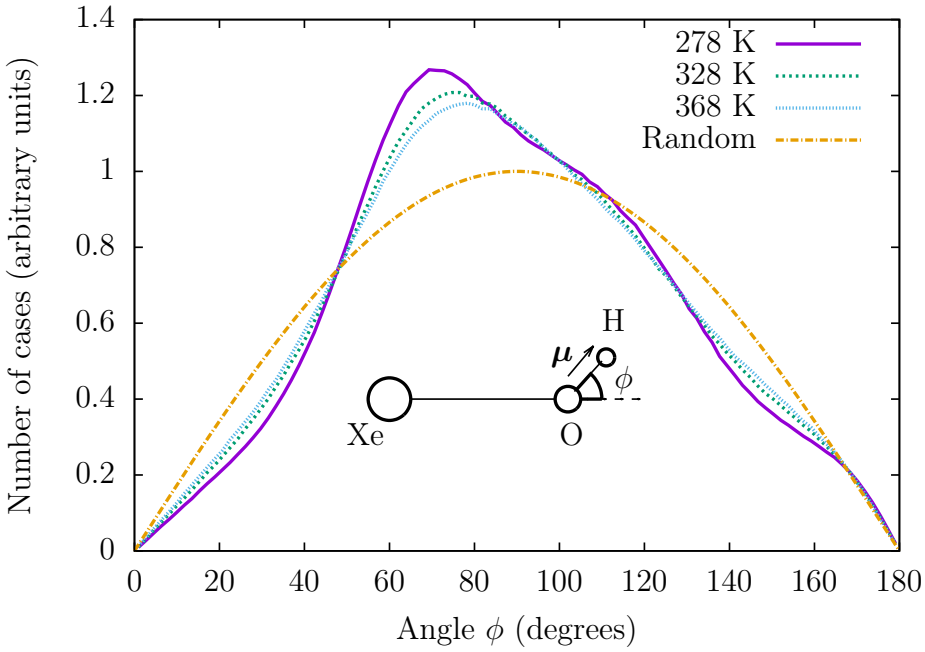

Figure 3.2: The distribution of the angles between the water dipole vector and the Xe–O direction calculated from the MD simulation trajectory for temperatures 278 K, 328 K and 368 K with a bin size of 1.8°. The distribution for an ideal, random orientational distribution is also included for comparison.

orientations around xenon. To accomplish this, the angle between the water dipole moment vector and the Xe – O direction was determined for each Xe – H_2O pair in all of the saved simulation geometries.[8] The water molecules included in the calculation were within the first solvation shell, *i.e.*, their distance from the xenon were 5.55 Å at maximum. The resulting angular distributions for three selected temperatures can be seen in Fig. 3.2 along with an even distribution for comparison. Even though there exist anomalies when compared to a random distribution, all of the possible angles are still present in the histogram. In other words, choosing just a single orientation when calculating the potential and the chemical shift for the Xe – H_2O dimer will not accurately describe the system, because all of the other orientations are very much present as well. Therefore, the binary chemical shift data to which the coefficients δ_n were fitted in the PCS approach, was determined somewhat arbitrarily as

$$\delta_{\text{pair}}^{\text{data}}(d) = \frac{\delta_1(d) + \delta_2(d) + \frac{1}{2}[\delta_{31}(d) + \delta_{32}(d)]}{3}, \tag{3.3}$$

where δ_i [not to be confused with the coefficients in Eq. (3.2)], refers to the geometry P_i in Fig. 3.3. The orientations P_i were chosen in such a way that the Xe – O direction was in all cases along one of the principal axes of the moment of inertia tensor of the water molecule and the total chemical shift was their average value. The geometries δ_{31} and δ_{32} have different weights for they correspond to the same principal axis and the chemical shift for that axis was interpreted to be their average. The used Xe – O distances ranged from 2.6 Å to 5.6 Å at intervals of 0.2 Å and from 5.6 Å to 8.0 Å at intervals of 0.4 Å.

[8] Every tenth geometry was saved in the simulation.

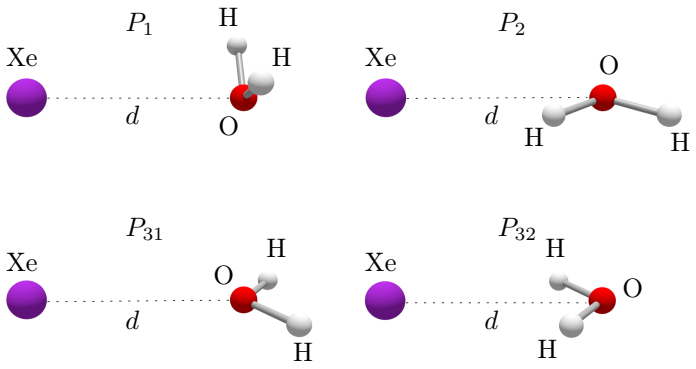

Figure 3.3: Orientations of the water molecule with respect to the xenon atom in calculation of the pairwise potential and chemical shift data for the semianalytical cavity model.

3.6 Semianalytical model of the water cavity

In order to have a more tangible interpretation for the interaction between the xenon atom and the surrounding water, a semianalytical approach was used in which the xenon atom was enclosed in a spherical shell thought of consisting of an even distribution of water molecules, illustrated in Fig. 3.4. The xenon atom is considered to be moving inside the cavity, as dictated by the potential energy as a function of the instantaneous displacement r from the center.

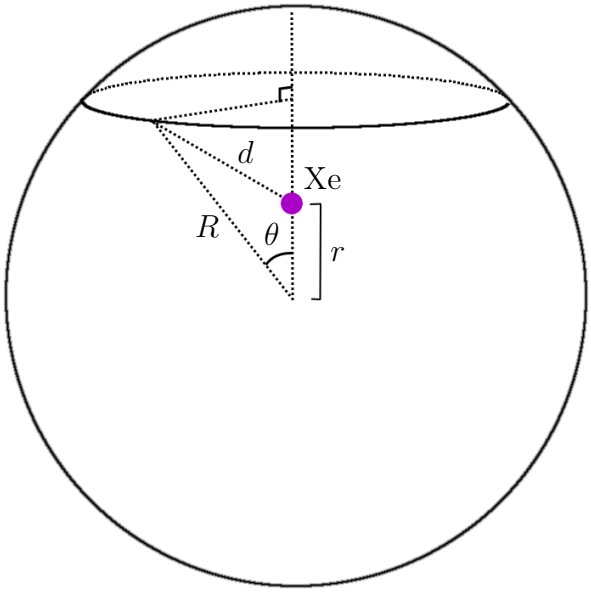

Figure 3.4: Illustration of the semianalytical water cavity model. Displacement of xenon from the center is r while its distance to the shell wall with a given angle θ is d. The radius of the sphere is R.

The probability density of a certain displacement r at a given temperature T is dictated by the Boltzmann distribution:

$$p(r,T) = \frac{e^{-V(r,T)/kT} r^2}{\int_0^{r_{\max}} e^{-V(r,T)/kT} r^2 \,\mathrm{d}r}, \tag{3.4}$$

where $V(r,T)$ is the potential energy. The expectation value of the chemical shift is then given by

$$\delta(T) = \int_0^{r_{\max}} \delta_{\mathrm{cav}}(r,T) p(r,T) \,\mathrm{d}r, \tag{3.5}$$

where $\delta_{\mathrm{cav}}(r,T)$ is the instantaneous chemical shift of the xenon atom due to the water cavity. Theoretically, the integration limit $r_{\max}$ should be the cavity radius R, but due to the abrupt increase of the potential energy function near that limit, the value $r_{\max} = 1.5$ Å was used instead, for at that point the probability density was in all cases already sufficiently close to zero.

3.6.1 Cavity radius and local water density

The cavity radius R was determined using the radial distribution functions (RDF) of the Xe–H_2O distances in the MD simulation, which were computed using the VMD code [65]. The RDFs are plotted in Fig. 3.5 along with the binary chemical shift functions, which will be discussed in more detail later on. The radius of the water cavity was determined somewhat arbitrarily as the expectation value of the Xe–H_2O distances up to the first minimum in the RDF, *i.e.*,

$$R(T) = \frac{\int_0^{r_1} d g(d,T) \,\mathrm{d}d}{\int_0^{r_1} g(d,T) \,\mathrm{d}d}, \tag{3.6}$$

where $r_1 = 5.5$ Å is the approximate distance to the first minimum, d is the Xe–O distance and $g(d,T)$ is the RDF. The surface number density of the water molecules was calculated as

$$\rho_S(T) = \frac{Z(T)}{4\pi R(T)^2} \tag{3.7}$$

where $Z(T)$ is the coordination number of the water molecules around xenon, *i.e.*, the expectation value of the number of water molecules whose distance from the xenon is r_1 at maximum. Z can be computed using the RDF as

$$Z(T) = 4\pi\rho(T) \int_0^{r_1} g(s,T) s^2 \,\mathrm{d}s, \tag{3.8}$$

where $\rho(T) = N/V(T) = 255/L(T)^3$ is the average number density of the water molecules in the simulation box of average side length $L(T)$. As was the case for the RDF, the coordination number was also determined with the VMD code.

3.6.2 Potential energy and chemical shift in the cavity

Assuming that the chemical shift and the Xe – H_2O potential energy are pairwise additive, they can be determined from the potential energy and the chemical shift curves calculated for the Xe – H_2O dimer in the following way. Let A_{pair} be either one of these qualities, expressed for the Xe – H_2O dimer in the form

$$A_{\mathrm{pair}}(d) = \sum_n \frac{A_n}{d^n}, \tag{3.9}$$

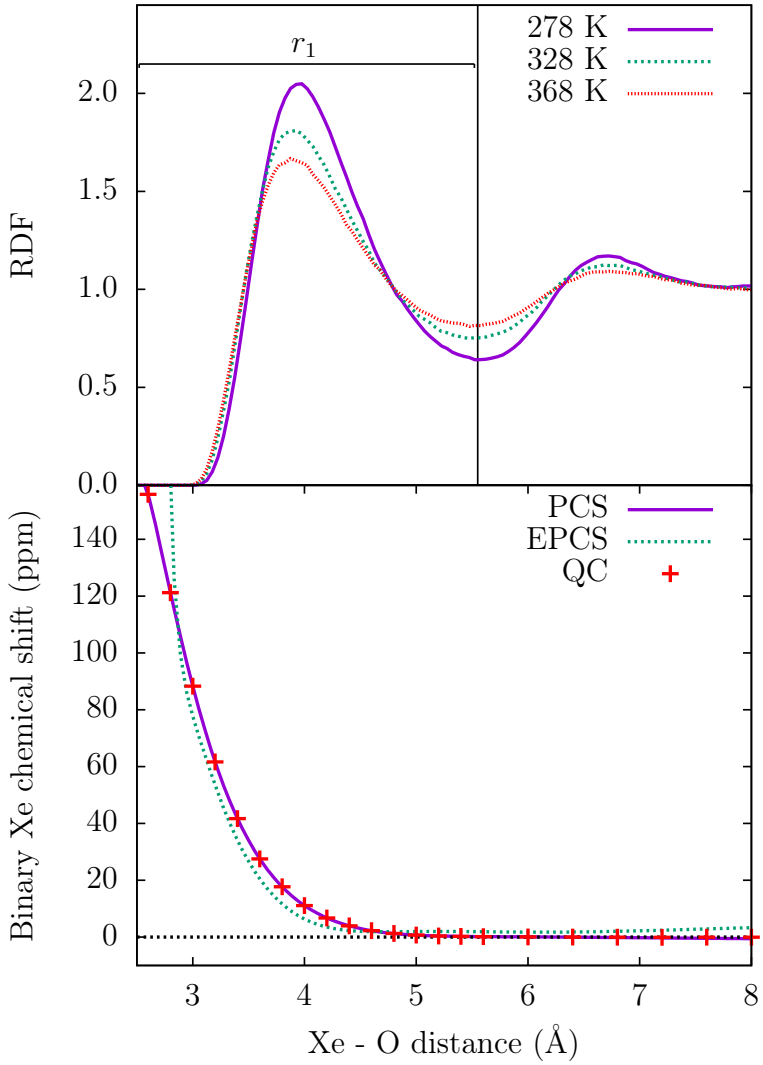

Figure 3.5: The radial distribution functions of the Xe–H_2O distances, calculated from the MD simulation data at different temperatures, as well as the binary xenon-water chemical shift as a function of the Xe – O distance. The terms PCS and EPCS refer to the pairwise additive binary chemical shift and the effective pair chemical shift, respectively.

where d is the distance between the xenon atom and the water molecule. In the cavity model, d corresponds to the distance between the xenon and the cavity wall, as depicted in Fig. 3.4. Through the cosine rule, the distance can be written as

$$d = \sqrt{R^2 + r^2 - 2rR\cos\theta} \tag{3.10}$$

and therefore, the total value of the quantity can be integrated in spherical coordinates as

$$\begin{aligned} A_{\text{total}}(r, R, T) &= \rho_S(T) \sum_n A_n R^2 \int_0^{2\pi} \mathrm{d}\phi \int_0^{\pi} \frac{\sin\theta \, \mathrm{d}\theta}{(R^2 + r^2 - 2rR\cos\theta)^{n/2}} \\ &\equiv \rho_S(T) \sum_n A_n I_n(r, R), \end{aligned} \tag{3.11}$$

where

$$\begin{aligned} I_n(r,R) &= R^2 \int_0^{2\pi} \mathrm{d}\phi \int_0^{\pi} \frac{\sin\theta \,\mathrm{d}\theta}{(R^2+r^2-2rR\cos\theta)^{n/2}} \\ &= 2\pi \frac{R}{r} \frac{(r-R)^2(r+R)^n - (R-r)^n(r+R)^2}{(n-2)(R^2-r^2)^n}, \end{aligned} \tag{3.12}$$

provided that $n > 2$. Because the NMR force fields introduced in Section 3.5 have the form (3.9) and the potential can also be expressed so, *i.e.*,

$$V_{\mathrm{pair}}(d) = \sum_n V_n / d^n, \tag{3.13}$$

the total potential energy and the chemical shift can be expressed as

$$V(r,T) = \rho_S(T) \sum_n V_n I_n(r, R(T)) \tag{3.14}$$

and

$$\delta_{\mathrm{cav}}(r,T) = \rho_S(T) \sum_n \delta_n I_n(r, R(T)). \tag{3.15}$$

Therefore, the expectation value (3.5) can be written as

$$\delta(T) = \rho_S(T) K(T), \tag{3.16}$$

where

$$K(T) = \sum_n \delta_n \int_0^{r_{\max}} I_n(r, R(T)) p(r,T) \,\mathrm{d}r. \tag{3.17}$$

The potential energy data used to fit $V_{\mathrm{pair}}(d)$ was determined in a similar manner as the PCS chemical shift function, namely

$$V_{\mathrm{pair}}^{\mathrm{data}}(d) = \frac{V_1(d) + V_2(d) + \frac{1}{2}[V_{31}(d) + V_{32}(d)]}{3}, \tag{3.18}$$

where, again, the term V_i corresponds to the geometry P_i in Fig. 3.3. The potential energy for the individual geometries was calculated using the AMOEBA potential energy which was previously fitted to the QC results. The data points used in the fit ranged between 2.0 Å and 7.0 Å with an interval of 0.1 Å.

3.6.3 Interpretation

The benefit of expressing the total chemical shift as a product of the form (3.16) is the fact that the surface density $\rho_S(T)$ corresponds directly to the local water density around the xenon atom. In other words, the interesting quality of the temperature dependence, namely the offset in the temperature of maximum chemical shift when compared to the temperature of maximum density, can be directly attributed to the term $K(T)$. Since the binary chemical shift function is the same in each temperature, the changes that occur in $K(T)$ can be interpreted to be due to collision energetics of the water molecules with xenon.

Chapter 4

Results and Discussion

4.1 Potential energy fitting

The fitted values for the acquired force-field parameters are listed in Table 4.1 along with the root mean square (RMS) error for each fit. The coefficients for the custom van der Waals potential functions in the fits 4 and 5 can be seen in Tables 4.2 and 4.3, respectively. The potential energy curves for the different fitting schemes along with the QC results can be seen in Fig. 4.1.

The deep potential well of G_5[1] can be seen to be the most problematic property to reproduce since, in the schemes 1–4, the fit differs by more than 0.1 kcal/mol at the lowest point. Only the fitting scheme 5, which used not only a modified van der Waals potential but also polarisability and Thole factor as parameters, does portray the well accurately. However, the acquired polarisability in the scheme was 10.5 Å^3, the largest value allowed. As this suggests, a better fit could have been achieved by allowing the polarisability to be higher, which would cause the simulation to eventually crash due to the divergence of the induction energy. Furthermore, the value is larger than the physical value (4.00 Å^3) by more than a factor of two. In other words, any physical interpretation for the fitting parameters has to be abandoned. For AMOEBA, this is not unheard of [66–69]. In Ref. [66], for instance, parameterising the Ni^{2+} ion charge along with polarisability was required and the polarisability acquired this way was also much too high when compared to the physical value.

[1] See Fig. 3.1.

Table 4.1: Parameters resulting from the different fitting schemes of the Xe – H_2O potential, along with the RMS error for each fit. R^0, ε, α and a are the AMOEBA force field parameters for the xenon atom as described in the section 2.1.2.

Fitting scheme[a]	R^0(Å^3)	ε (kcal/mol)	α(Å^3)	a	RMS (kcal/mol)
1: vdW	4.15	2.362	4.00[b]	0.390[b]	0.934
2: vdW + pol	4.22	0.630	7.38	0.390[b]	0.902
3: vdW + pol + Thole	4.28	0.551	9.74	0.600	0.732
4: vdWf	[c]	[c]	4.00[b]	0.390[b]	0.790
5: vdWf + pol + Thole	[d]	[d]	10.50	0.422	0.543

[a] vdW = AMOEBA van der Waals potential, vdWf = modified van der Waals potential, pol = polarisability, Thole = the Thole charge distribution parameter.

[b] Values fixed to the defaults mentioned in Section 3.2.

[c] The coefficients used in the van der Waals function can be found in Table 4.2.

[d] The coefficients used in the van der Waals function can be found in Table 4.3.

Table 4.2: Coefficients C_n (kcal/mol $\cdot$ Å^n) for the Xe – H_2O potential energy function obtained for the van der Waals interaction in fitting scheme 4.

n	Xe-O	Xe-H
6	1310689.71	-218214.476
7	-35429966.6	4937545.52
8	396196927	-46027048.0
9	-2340855590	225206026
10	7690972840	-609301598
11	-13309291700	864388166
12	9477377670	-502548480

Table 4.3: Coefficients C_n (kcal/mol $\cdot$ Å^n) for the Xe – H_2O potential energy function obtained for the van der Waals interaction in fitting scheme 5.

	Xe-O		Xe-H		
n	$r < 4.8$ Å	$r > 4.8$ Å	$r < 2.6$ Å	2.6 Å $< r <$ 4.8 Å	$r > 4.8$ Å
6	801555.018	4876.79102	24.7660805302	-222292.216	-696.652497
7	-20773611.3	-	-	4966925.83	-
8	225279395	-275293.311	-	-45687194.5	452.836189
9	-1302803650	-	-	220688180	-
10	4218217740	4079268.19	-	-590226520	102193.118
11	-7227315890	-	-	829217086	-
12	5112459130	-16232604.1	125052.162836	-478390319	-340001.857

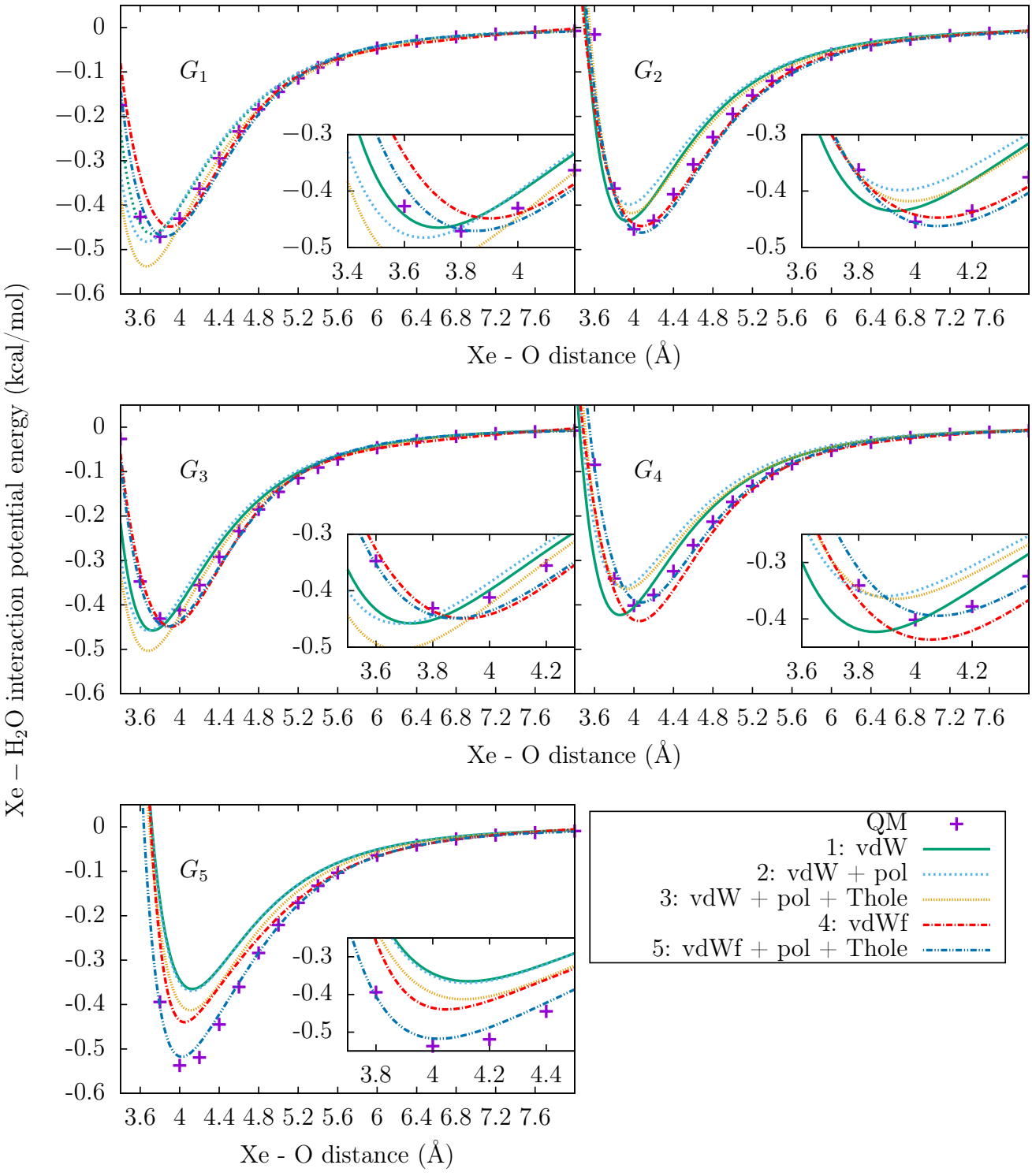

Figure 4.1: Fits of the $Xe - H_2O$ potential to the *ab initio* calculations (QC) with the following parameters adjusted. 1: AMOEBA van der Waals parameters; 2: van der Waals and polarisability; 3: van der Waals, polarisability and Thole parameters; 4: coefficients C_n in the van der Waals potential of Eq. (3.1); 5: polarisability, Thole factor and the coefficients C_n. The labels $G_1, G_2, ...$ correspond to the orientations shown in Fig. 3.1.

4.2 Xenon chemical shift

4.2.1 QC simulation snapshots

The average nonrelativistic xenon chemical shifts that were computed from the snapshots extracted from the MD simulations are listed in Table 4.4 and the temperature dependence is plotted in Fig. 4.2. General features of the chemical shift for various computational methods as well as the experimental values for H_2O and D_2O are shown in Table 4.5.

Fig. 4.2 shows immediately that the maximum of the chemical shift is reproduced by the QC averaging. With the nonrelativistic treatment, however, its overall magnitude remains approximately 40 ppm lower than the experimental values. This difference can to a large degree be explained by the nonrelativistic treatment and the incompleteness of the basis set, which is to be shown in the next section. The temperature of the maximum lies at 334.7 K, while the experimental values are 311.13 K and 315.33 K for H_2O and D_2O, respectively. In other words, the QC averaged maximum temperature is 24.6 K or 19.4 K higher than what is found experimentally. This is not surprising since for the original AMOEBA water model (H_2O), the temperature of maximum density is 13 K or 6 K higher when compared to real H_2O or D_2O, respectively [9]. The AMOEBA water density also changes faster as a function of temperature than the real water density [9], which explains the steeper chemical shift slope in this case.

The classical simulation of H_2O behaves more like D_2O than H_2O. The physical difference between H_2O and D_2O can be attributed to purely quantum-mechanical isotope effects, which cannot be reproduced in a classical simulation. Due to the heaviness of deuterium, D_2O solution is the more classical system and, therefore, expected to have properties similar to a classical simulation.

Table 4.4: Number of simulation snapshots and the computed average ^{129}Xe chemical shifts [nonrelativistic DFT(BHandHLYP) calculation with basis set def-TZVP for O and H and $27s25p21d4f$ for Xe] at several temperatures, along with the standard error of mean (SEM), statistical inefficiency s [70] and the estimated statistical error $\Delta\delta$. The error was calculated as $\Delta\delta = \sqrt{s} \cdot \Delta\delta^{\mathrm{SEM}}$ [70].

T(K)	N	δ(ppm)	$\Delta\delta^{\mathrm{SEM}}$(ppm)	s	$\Delta\delta$(ppm)
278	2706	136.0	0.7	4.5	1.5
288	2685	139.8	0.8	2.2	1.1
298	2687	142.7	0.8	2.5	1.2
308	2687	144.7	0.8	1.8	1.1
318	2686	145.5	0.8	1.2	0.9
328	2686	146.5	0.9	1.3	1.0
338	2687	146.1	0.9	1.3	1.0
348	2686	146.8	0.9	1.0	0.9
358	2686	144.9	0.9	1.0	0.9
368	2684	143.1	0.9	1.2	1.0

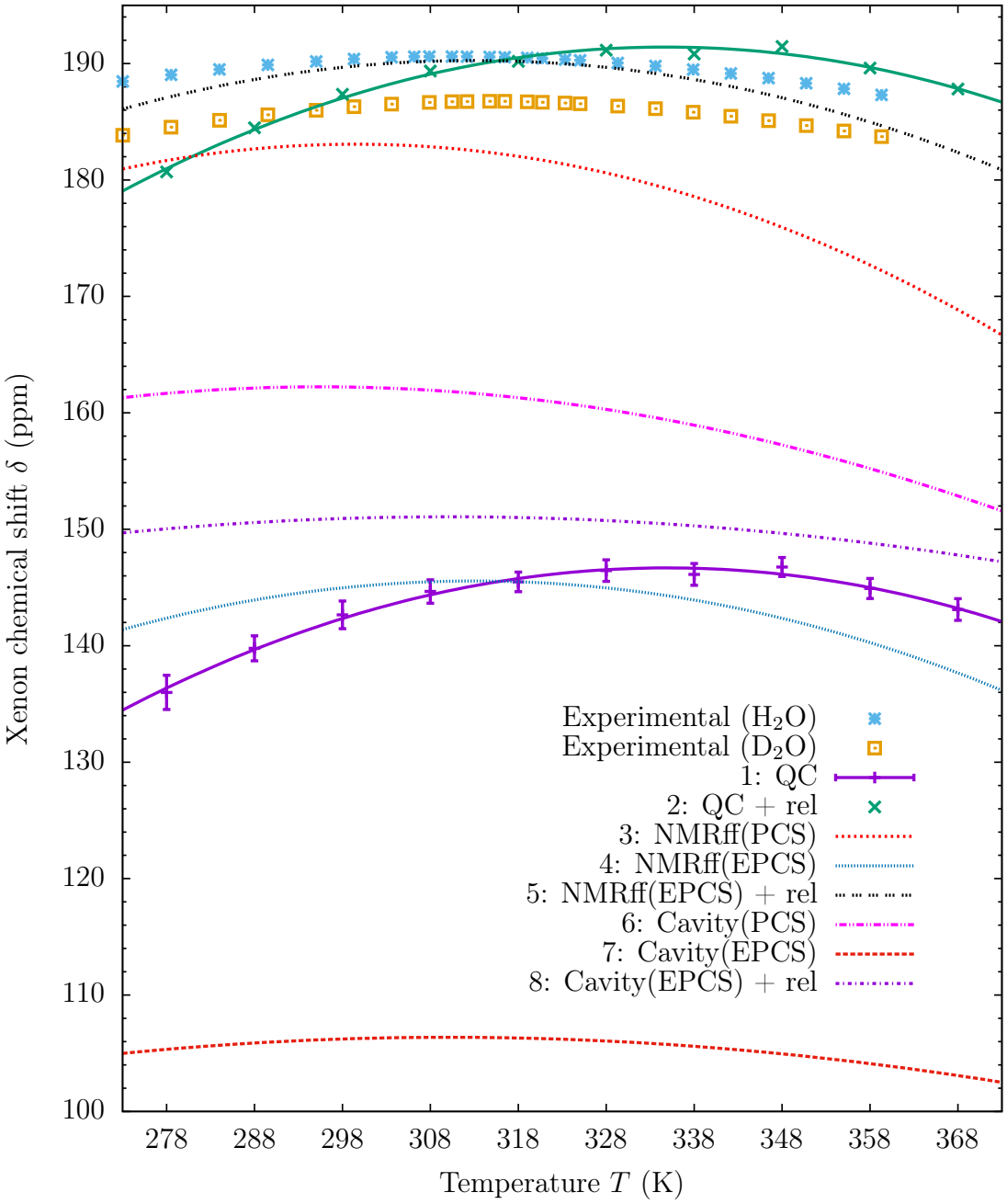

Figure 4.2: Calculated ^{129}Xe chemical shift in an aqueous solution of atomic Xe as a function of temperature. Results from methods 1-8 (please refer to Table 4.5) and NMR experiments in normal (H_2O) and heavy water (D_2O) [71]. For methods 3-5, only the least-squares fit is plotted.

Table 4.5: Experimental and computational values of the maximum value $\delta_{\max}$ of the ^{129}Xe chemical shift in aqueous solution of atomic Xe, the temperature $T_{\max}$ at which it occurs and the "curvature" a_δ of the chemical shift, obtained with different methods. The parameters $\delta_{\max}$, $T_{\max}$ and a_δ were determined by fitting the shift vs. temperature data to a quadratic polynomial $\delta(T) = \delta_{\max} - a_\delta(T - T_{\max})^2$.

Method[a]	$\delta_{\max}$ (ppm)	$T_{\max}$ (K)[b]	$a_\delta \left(\frac{10^{-3}\text{ppm}}{K^2}\right)$
Experimental (H_2O)	190.573 ± 0.001[c]	311.13 ± 0.13[c]	1.4409 ± 0.013[c]
Experimental (D_2O)	186.707 ± 0.014[c]	315.33 ± 0.14[c]	1.6029 ± 0.018[c]
1. QC	146.7 ± 0.2[c]	334.7 ± 1.0[c]	3.3 ± 0.2[c]
2. QC + rel[d]	191.4 ± 0.2[c]	334.7 ± 1.0[c]	3.3 ± 0.2[c]
3. NMRff(PCS)	183.1 ± 0.4[c]	299 ± 4[c]	3.0 ± 0.4[c]
4. NMRff(EPCS)	145.6 ± 0.4[c]	313 ± 2[c]	2.6 ± 0.4[c]
5. NMRff(EPCS) + rel[d]	190.3 ± 0.4[c]	313 ± 2[c]	2.6 ± 0.4[c]
6. Cavity (PCS)	162.1	295.3	1.73
7. Cavity (EPCS)	106.3	310.4	0.97
8. Cavity (EPCS) + rel[d]	151.0	310.4	0.97

[a] 1: Nonrelativistic QC snapshot calculations; 2: QC snapshot calculations with *a posteriori* relativistic correction; 3: NMR force field calculation from the MD snapshots in a pairwise-additive manner using the PCS approach; 4: NMR force field calculation with the EPCS approach; 5: NMR force field calculation with the EPCS approach with *a posteriori* relativistic correction; 6: The semianalytical cavity model with the PCS approach and 7: with the EPCS approach; 8: Cavity model with the EPCS approach with *a posteriori* relativistic correction.

[b] The density maximum of the AMOEBA water model occurs at 290 K for a classical MD simulation [9]. The experimental density maximum occurs at 277.13 K and 284.34 K for H_2O and D_2O, respectively [6].

[c] The statistical error acquired by the least-squares fit.

[d] Relativistic offset as described in section 4.2.1.

Relativistic corrections

Table 4.6 lists the relativistic ADF chemical shift of xenon in the twenty chosen example snapshots. On average, the relativistic effects add (30.3±5.9) ppm[2] to the nonrelativistic results with the jcpl/TZP basis set. Furthermore, the improvement of basis set alone from $27s25p21d4f$/def-TZVP to jcpl/TZP adds (14.4±3.0) ppm to the chemical shift and when both effects are taken into account, the difference is (44.7±7.0) ppm. Therefore, the total effect of the basis set/relativistic contributions was estimated by implementing a systematic offset off +44.7 ppm at each temperature. Fig. 4.2 shows that this brings the overall magnitude of the chemical shift based on the QC calculations on MD snapshots to the same level as the experiment.

[2] Average ± standard deviation (STD).

Table 4.6: Results in ppm for the relativistic (SR and ZORA) and nonrelativistic (NR) ADF calculations for the ^{129}Xe chemical shift for twenty selected MD snapshots throughout the simulation of the aqueous solution of atomic xenon at different temperatures. T represents the temperature of the trajectory from which the snapshot was taken, either the configuration of minimum energy (Min. en.) or randomly chosen (Rand.). The average value and the standard deviation (STD) are also represented for the chemical shifts at each level of theory.[a]

T	Snapshot	NR-TM	NR-ADF	SR-ZORA	SO-ZORA	$\Delta_{\mathrm{NR}}{}^{b}$	$\Delta_{\mathrm{rel}}{}^{c}$	$\Delta_{\mathrm{NR+rel}}{}^{d}$
278	Min. en.	76.8	87.8	102.6	109.2	11.0	21.5	32.5
288	Min. en.	137.4	155.6	177.4	185.3	18.2	29.7	47.9
298	Min. en.	146.7	162.2	182.9	190.5	15.5	28.3	43.8
308	Min. en.	173.3	182.6	211.5	222.7	9.3	40.1	49.5
318	Min. en.	141.3	158.6	179.7	188.4	17.3	29.8	47.1
328	Min. en.	123.8	137.4	156.4	164.2	13.6	26.8	40.4
338	Min. en.	79.7	97.6	112.3	117.8	17.9	20.2	38.1
348	Min. en.	132.2	146.2	168.0	177.6	14.0	31.3	45.3
358	Min. en.	156.5	175.3	200.5	211.9	18.8	36.5	55.3
368	Min. en.	246.5	261.9	295.3	304.9	15.4	42.9	58.4
278	Rand.	165.0	179.9	203.4	212.9	14.9	33.1	47.9
288	Rand.	203.2	217.7	243.4	252.6	14.4	34.9	49.4
298	Rand.	167.9	176.0	196.1	203.2	8.1	27.2	35.2
308	Rand.	123.7	138.7	158.3	166.6	15.0	27.9	42.9
318	Rand.	200.4	213.8	239.5	249.9	13.4	36.1	49.6
328	Rand.	134.3	150.5	173.2	182.3	16.2	31.8	48.0
338	Rand.	131.2	148.6	169.3	178.0	17.4	29.4	46.8
348	Rand.	155.7	170.3	191.0	197.9	14.6	27.6	42.3
358	Rand.	163.6	177.5	199.8	208.7	13.9	31.2	45.1
368	Rand.	97.2	105.7	120.1	125.8	8.6	20.0	28.6
	Average	147.8	162.2	184.0	192.5	14.4	30.3	44.7
	STD	39.7	39.9	44.0	45.1	3.0	5.9	7.0

[a] NR-TM: nonrelativistic Turbomole/Dalton-calculated shifts used for the snapshots.
NR-ADF: nonrelativistic ADF.
SR-ZORA: scalar-relativistic (SR) part of the ZORA results.
SO-ZORA: both the SR and spin–orbit (SO) parts included at the ZORA level.

[b] Difference between NR-ADF and NR-TM.

[c] Difference between SO-ZORA and NR-ADF.

[d] Difference between SO-ZORA and NR-TM.

4.2.2 NMR force field

The NMR force field coefficients δ_n [Eq. (3.2)] for both the PCS and EPCS parameterisations can be seen in Table 4.7. The chemical shifts were calculated at each simulation temperature in a binary pairwise-additive manner with both approaches using the same snapshots as for the QC calculations and the resulting plot can be seen in Fig. 4.2. The EPCS approach gives expectedly the same overall magnitude of the chemical shift as the QC calculations, while the PCS chemical shift is approximately 40 ppm higher. This means that the xenon chemical shift in the liquid water environment cannot be treated quantitatively with a strictly pairwise-additive chemical shift function. However, the important feature of the temperature dependence, namely the existence of a maximum, is accomplished by both approaches, which suggests that treating the total chemical shift as a sum of pairwise contributions between xenon and water molecules can be used qualitatively to explain the phenomenon.

With both force field parameterisations, the temperature of the maximum is significantly lower than the QC calculations predict, even with the EPCS approach, despite the fact that it was parameterised with the very same data. This proves that the pairwise-additive treatment has its limitations and that the beyond-binary interactions can have a significant role in the location of the chemical shift maximum. The fact that the PCS chemical shift is apparently more successful when compared to the experimental values is due to the cancellation of two errors, namely the neglect of nonbinary intermolecular interactions (which are implicitly included in the EPCS approach) as well as relativistic effects. However, when the systematic relativistic offset of 44.7 ppm is added to the EPCS results, its agreement with experiment is better than with the PCS parameterisation. Morever, Fig. 4.2 shows that it gives a chemical shift curve almost identical to the experimental data for H_2O. However, this bears no real significance since the "parent" data of the parameterisations is the QC snapshot data, which should remain as the point of reference.

Table 4.7: Coefficients δ_n for the chemical shift functions used in both the NMR force field analysis of the MD snapshots and the semianalytical cavity model, as well as the pair potential coefficients V_n used only in the semianalytical cavity model. PCS and EPCS stand for binary and effective pair chemical shift function, respectively

		$\delta_n(\text{ppm} \cdot \text{Å}^n)$	
n	$V_n(\text{kcal/mol} \cdot \text{Å}^n)$	PCS	EPCS
6	509813.157	-42300792.126	331491127
7	-14192000.4	1276710522.22	-10918170100
8	166263818	-16547206266.3	155848618000
9	-1074024180	120446322075.0	-1258224540000
10	4179852730	-539607787650.0	6282948000000
11	-10045391900	1527147215620	-19876027800000
12	14613195300	-2671464021010	38920341400000
13	-11816774200	2644810217460	-43157292300000
14	4083563200	-1135749395950	20761184000000

The inaccuracy of the xenon chemical shift when using a strictly binary pairwise-additive chemical shift function has been encountered before in Xe_n clusters [72]. In Ref. [72], a similar effective pair chemical shift function as in the present case was used for Xe–Xe interactions as the purely binary chemical shift function was found to overestimate the total chemical shift increasingly with the cluster size.

The pair chemical shift functions are plotted in Fig. 3.5 as functions of Xe – O distance. The PCS approach can be seen to have larger values throughout the Xe – O distances that lie within the first solvation shell, *i.e.*, the region around the first peak of the RDF. This difference is maximally 8 ppm and it explains the large gap between the total chemical shifts resulting from the PCS and EPCS parameterisations. Table 4.5 shows that there is also a 14 K difference in the temperatures at the chemical shift maxima $T_{\max}$ between the two parameterisations. This shows that $T_{\max}$ is very sensitive to subtle changes in the pair chemical shift function, which can also be seen in the case of the semianalytical cavity model, as shown below.

4.2.3 Semianalytical cavity model.

In Fig. 4.3, the cavity radius R and the coordination number Z are plotted as functions of temperature. The coordination decreases with temperature and it drops from 22.0 at 278 K to 20.5 at 368 K. The overall magnitude of the coordination number is consistent with the value of 21.5 obtained by Schnitker and Geiger [73] who used the ST2 water model [74] at the temperature of 295 K and pressure of 1.03 atm. The cavity radius, on the other hand, does not change much and its values only differ by maximally 0.02 Å. However, it does have a shallow minimum at 292 K, close to the density maximum of the AMOEBA water at 290 K [9].

The coordination number was expressed as

$$Z(T) = Z_0 - a_Z(T - T_Z^{\max})^2, \tag{4.1}$$

for the purposes of the semianalytical cavity model, where $Z_0 = 21.989$, $T_Z^{\max} = 260.56$ K and $a_Z = 0.000126697$ K^{-2}. Z_0, $T_Z^{\max}$ and a_Z were determined by least-squares fitting to the MD data. In a similar fashion, the cavity radius was

$$R(T) = R_0 + a_R(T - T_R^{\min})^2, \tag{4.2}$$

where $R_0 = 4.2675$ Å, $a_R = 3.57311 \cdot 10^{-6}$ Å/K^2 and $T_R^{\min} = 292.34$ K.

The probability density p and the xenon chemical shift function δ_{cav} are displayed in Fig. 4.4 as functions of distance from the cavity center r. The xenon chemical shift increases monotonically as a function of r due to the sharp increase in the binary chemical shift function at small distance to the water molecule. The probability density has a maximum at around $r = 0.6$ Å and, with increasing temperature, it decreases in magnitude and its location shifts to a higher value of r. p drops to zero at around $r = 1.2$ Å at all temperatures, which justifies the choice of the integration limit $r_{\max} = 1.5$ Å.

Eq. (3.5) was used to calculate the total chemical shift at the temperature interval of interest and the results are plotted in Fig. 4.2. Even though the temperatures of the maximum are approximately the same when compared to the corresponding values calculated straightforwardly with the NMR force field method described above, the overall magnitude of the chemical shift is 10 – 20 ppm lower with the PCS parameterisation and 30 – 40 ppm lower with the EPCS parameterisation. Even if the relativistic 44.7 ppm

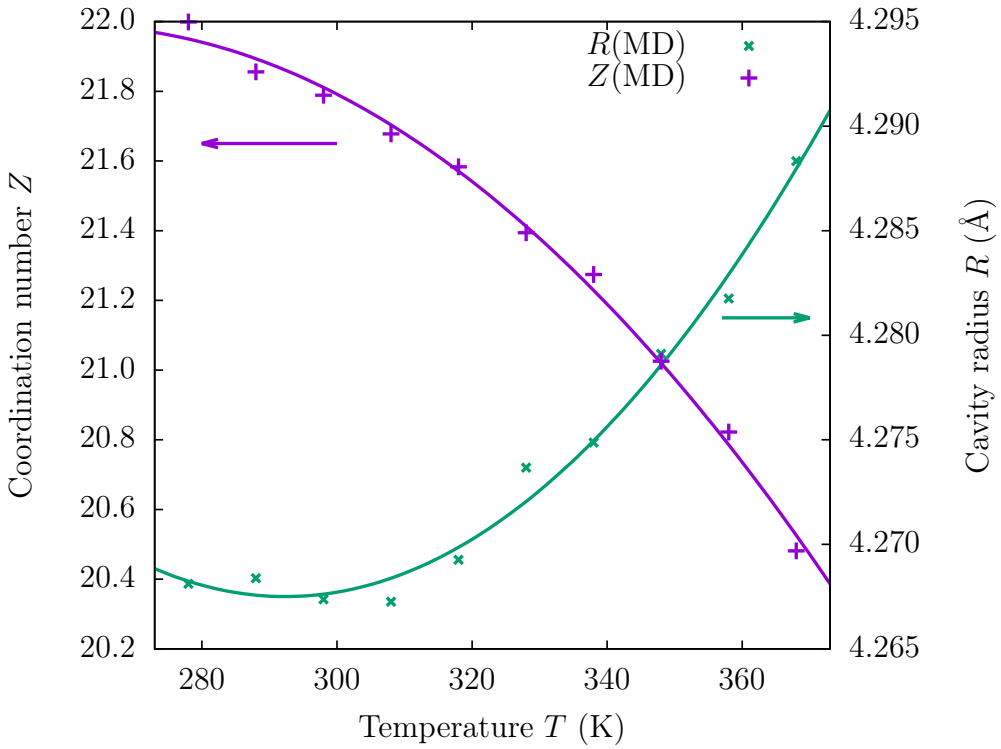

Figure 4.3: Coordination number Z of the xenon atom and the cavity radius of R in the semianalytical cavity model, as functions of temperature, along with the fitted quadratic polynomials [Eqs. (4.1) and (4.2)]. Z and R were calculated from the MD simulation trajectory as described by Eqs. (3.8) and (3.6), respectively.

offset is added to the EPCS parameterisation, the magnitude of the chemical shift remains more than 30 ppm lower than the experimental values. The most probable cause for this is the rather arbitrary way that the cavity radius R was defined; changing the integration limit r_1 in Eq. (3.6) can have abrupt changes in the overall magnitude of the chemical shift. If $r_1 = 4.9$ Å, for example, it would result in $T_{\max} = 334,7\ K$, $\delta_{\max} = 187.3$ ppm and $a_\delta = 1.80 \cdot 10^{-3}\,\mathrm{ppm/K^2}$ for the EPCS chemical shift with the relativistic offset, which is comparable to the result given by the QC results with the relativistic correction. This also proves that the relative flatness of the chemical shift curve when compared to the corresponding NMR force field result can be attributed to the selection of R. This can be explained by the fact that RDF reaches its maximum at around distance 3.9 Å which is less than the cavity radius $R \approx 4.2$ Å. When the temperature rises, larger displacements r become increasingly probable for the xenon atom, but due to the fact that the cavity wall is bit further away in the semianalytical model than the MD data would suggest, the changes are not as abrupt.

As was explained in Section 3.6.2, the semianalytical cavity model represents the total chemical shift as a product of two factors, namely the surface number density $\rho_S(T)$ of the water molecules at the cavity surface and the interaction factor $K(T)$. These quantities are plotted individually as functions of temperature in Fig. 4.5, as well as the resulting chemical shift functions. Not surprisingly, the surface density ρ_S behaves in a similar fashion as the coordination number, *i.e.*, decreasing nonlinearly with temperature, since the cavity radius R varies very little. The function $K(T)$, on the other hand, is an ascending function in both the PCS and EPCS approaches. For the EPCS parameterisation, K

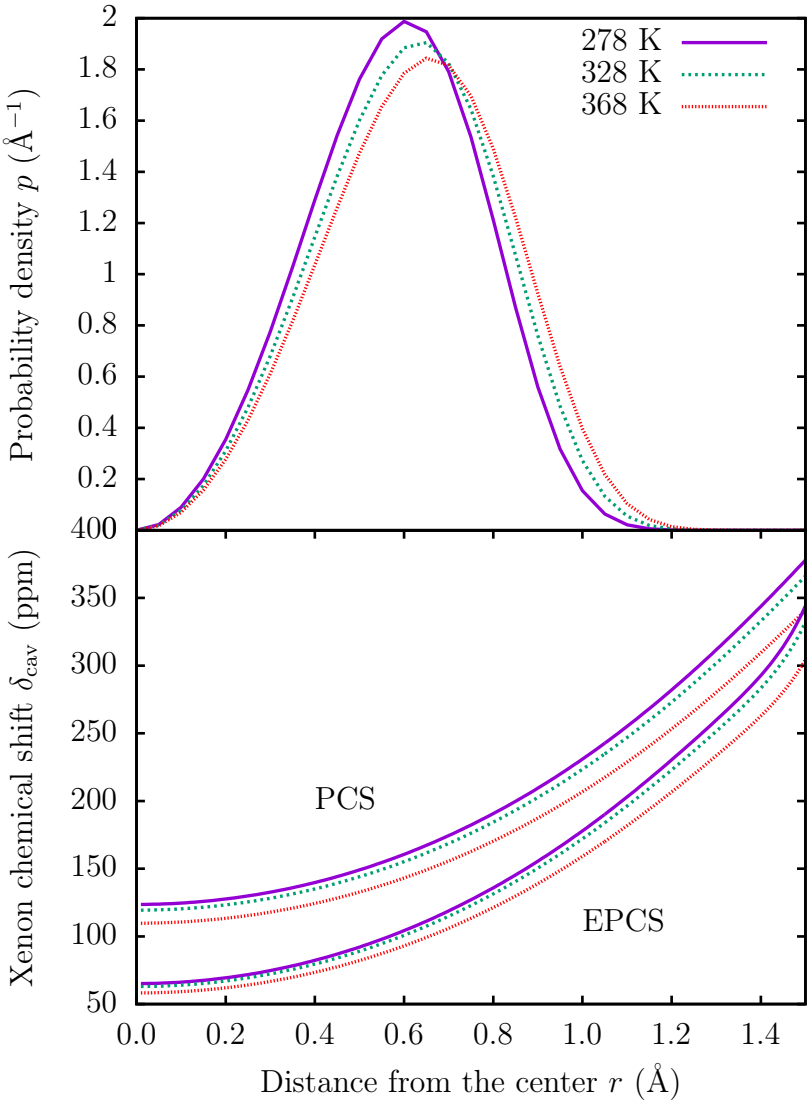

Figure 4.4: Probability density p and chemical shift δ_{cav} of xenon in the qualitative cavity model, described by Eqs. (3.4) and (3.15), respectively, as functions of the distance from the center, calculated at temperatures 278 K, 328 K and 368 K.

behaves mostly linearly but for the PCS parameterisation, K has a maximum at 357 K. In both cases, multiplying the surface density ρ_S with K results in a function whose maximum value lies at a temperature higher than the temperature of the extrapolated maximum of the surface density (267 K).

Fig 4.5 shows that with the cavity model, the chemical shift function resulting from the EPCS parameterisation has a higher temperature of maximum chemical shift than the PCS parameterisation but a smaller curvature. Both of these facts can be attributed to the overall difference in magnitude between the functions K with the two approaches. The fact that the PCS K has inherent curvature makes the PCS chemical shift function even sharper.

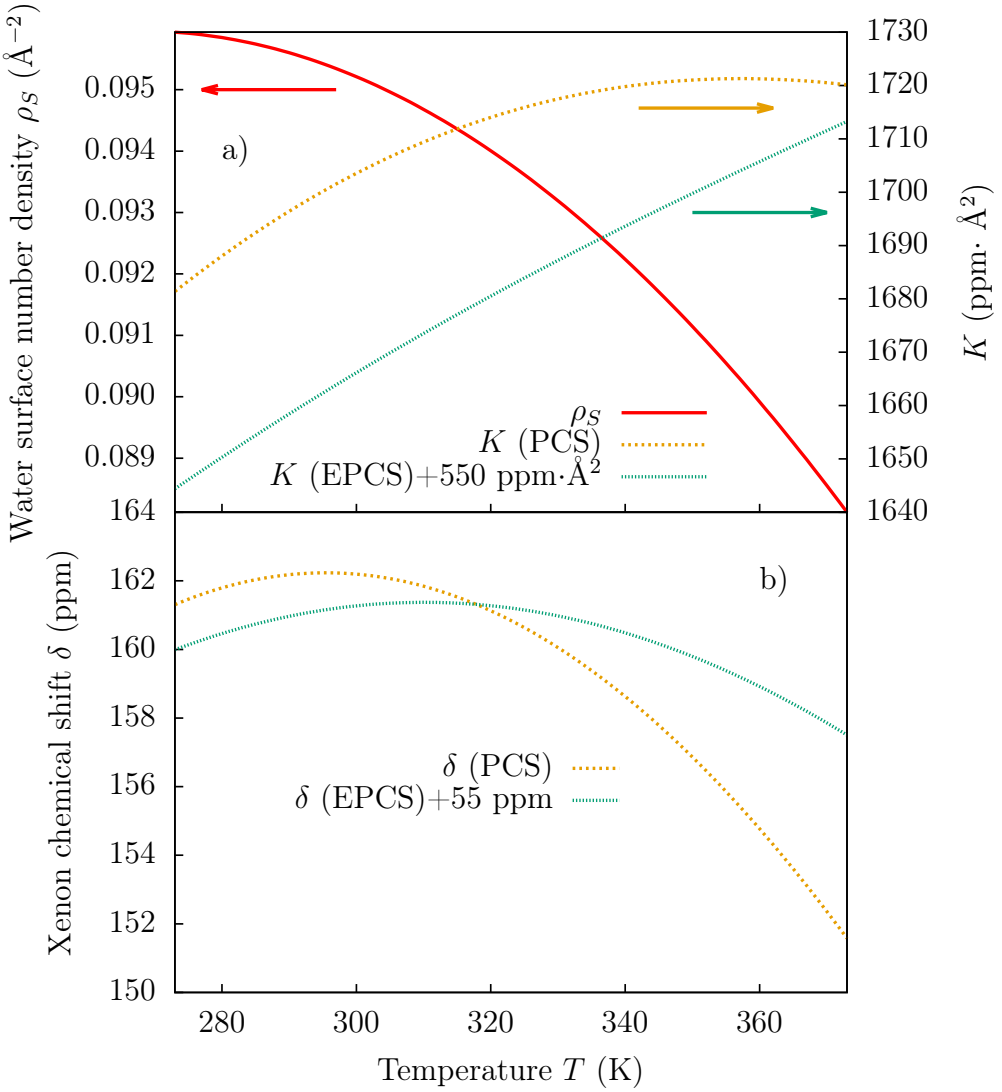

Figure 4.5: a) Solvent density at the surface of the cavity ρ_S and the function K, defined by Eqs. (3.7) and (3.17), as well as b) their product, the xenon chemical shift, as functions of temperature. PCS and EPCS refer to the strictly binary and effective chemical shift functions, respectively. To render the comparison easier, offsets of 550 ppm×Å^2 and 55 ppm were added to the EPCS K and δ, respectively.

Chapter 5

Conclusions

The temperature dependence of the chemical shift of a xenon atom in an aqueous solution was qualitatively reproduced in this thesis in three distinct ways. Firstly, by calculating the chemical shift quantum-chemically for a number of snapshots from an MD simulation trajectory and then averaging them specifically for ten different temperatures. Secondly, by calculating the chemical shift pairwise-additively from the MD simulation geometries with the NMR force field approach. Third, by interpreting the water around the xenon atom as a spherical shell consisting of an even distribution of water molecules and finding the temperature dependence in terms of the local water density around xenon and the binary xenon-water interaction function. All approaches are able to reproduce the most distinct feature of the chemical shift, a maximum for the chemical shift that is at higher temperature than the corresponding temperature of maximum density of pure water.

The QC snapshot averaging predicts a temperature of maximum chemical shift that is a lot higher than the experiment suggests, in keeping with the higher temperature of maximum density of the AMOEBA water. If *a posteriori* relativistic offset is added, the overall magnitude of the chemical shift is reproduced. The NMR force field approach produces the maximum at temperatures closer to the experimental value and, with EPCS parameterisation with the relativistic offset, reproduces the experimental chemical shift curve most accurately.

The semianalytical cavity model provides a qualitative way of understanding the difference in the temperatures of maximum density and maximum chemical shift. The total chemical shift can be interpreted as a product of two terms: the local water density around the xenon atom and an interaction term consisting of the binary xenon-water chemical shift function and the collision energetics. The latter term ascends with temperature and multiplication with the decreasing density causes the shift in the maximum. In most liquid environments, the xenon chemical shift is a decreasing function of temperature [75, 76], portraying the linear temperature dependence of the liquid density. In principle, the chemical shift could have a maximum in liquids other than water as well, since the maximum would occur even if the decrease is linear as long as the contribution of the collision energetics increases with temperature. However, no maximum can be observed in most other liquids. A possible explanation for this is that water is special because the location of the maximum happens to be within the temperature range of its liquid phase; if this is not the case for most other liquids, then the absence of the maximum is accounted for.

Bibliography

[1] C. J. Jameson, A. K. Jameson, & S. M. Cohen: Second virial coefficient of ^{129}Xe chemical shielding in mixtures of Xe with spherical top molecules CH_4, CF_4, and SiF_4, *J. Chem. Phys.* **65**, (1976), 3401–3406.

[2] P. Morgado, K. Shimizu, J. M. S. S. Esperanca, P. M. Reis, L. P. N. Rebelo, J. N. Canongia Lopes, *et al.*: Using Xe-129 NMR to probe the structure of ionic liquids, *J. Phys. Chem. Lett.* **4**, (2013), 2758–2762.

[3] J. Jokisaari, P. Diehl, & O. Muenster: ^{129}Xe NMR in liquid-crystals: Detection of induced smectic phases in binary-mixtures of nematic liquid-crystals by use of xenon gas as a probe, *Mol. Cryst. Liq. Cryst.* **188**, (1990), 189–196.

[4] J. P. Jokisaari, G. R. Luckhurst, B. A. Timimi, J. Zhu, & H. Zimmermann: Twist-bend nematic phase of the liquid crystal dimer CB7CB: Orientational order and conical angle determined by ^{129}Xe and ^{2}H NMR spectroscopy, *Liq. Cryst.* **42**, (2015), 708–721.

[5] V.-V. Telkki, J. Lounila, & J. Jokisaari: Determination of pore sizes and volumes of porous materials by ^{129}Xe NMR of xenon gas dissolved in a medium, *J. Phys. Chem. B* **109**, (2005), 24343–24351.

[6] G. S. Kell: Precise representation of volume properties of water at one atmosphere, *J. Chem. Eng. Data* **12**, (1967), 66–69.

[7] T. Helgaker, M. Jaszuński, & K. Ruud: Ab initio methods for the calculation of NMR shielding and indirect spin-spin coupling constants, *Chem. Rev.* **99**, (1999), 293–352.

[8] P. Ren, & J. W. Ponder: Polarizable atomic multipole water model for molecular mechanics simulation, *J. Phys. Chem. B* **107**, (2003), 5933–5947.

[9] P. Ren, & J. W. Ponder: Temperature and pressure dependence of the AMOEBA water model, *J. Phys. Chem. B* **108**, (2004), 13427–13437.

[10] P. Peuravaara: *Ksenon-vesiliuoksen rakenneominaisuuksien lämpötilariippuvuus molekyylidynamiikkasimulaation avulla*, Bachelor's thesis, University of Oulu, 2015.

[11] D. Frenkel & B. Smit: *Understanding molecular simulation: From algorithms to applications*, 2nd ed., San Diego: Academic Press, 2002.

[12] M. P. Allen & D. J. Tildesley: *Computer simulation of liquids*, New York: Clarendon Press, 1989.

[13] D. Beeman: Some multistep methods for use in molecular dynamics calculations, *J. Comput. Phys.* **20**, (1976), 130–139.

[14] S. Nosé: A molecular dynamics method for simulations in the canonical ensemble, *Mol. Phys.* **52**, (1984), 255–268.

[15] W. G. Hoover: Canonical dynamics: Equilibrium phase-space distributions, *Phys. Rev. A* **31**, (1985), 1695–1697.

[16] B. Brooks: *Algorithms for molecular dynamics at constant temperature and pressure*, DCRT Report, 1988.

[17] S. E. Feller, Y. Zhang, R. W. Pastor, & B. R. Brooks: Constant pressure molecular dynamics simulation: The Langevin piston method, *J. Chem. Phys.* **103**, (1995), 4613–4621.

[18] D. J. Griffiths & R. College: *Introduction to electrodynamics*, 3rd ed., New Jersey: Prentice Hall, 1999.

[19] P. W. Atkins & R. S. Friedman: *Molecular quantum mechanics*, 5th ed., New York: Oxford University Press, 2011.

[20] B. G. Levine, J. E. Stone, & A. Kohlmeyer: Fast analysis of molecular dynamics trajectories with graphics processing units—Radial distribution function histogramming, *J. Comput. Phys.* **230**, (2011), 3556–3569.

[21] J. W. Ponder, C. Wu, P. Ren, V. S. Pande, J. D. Chodera, M. J. Schnieders, *et al.*: Current status of the AMOEBA polarizable force field, *J. Phys. Chem. B* **114**, (2010), 2549–2564.

[22] B. Thole: Molecular polarizabilities calculated with a modified dipole interaction, *Chem. Phys.* **59**, (1981), 341–350.

[23] P. Hohenberg & W. Kohn: Inhomogeneous electron gas, *Phys. Rev.* **136**, (1964), B864–B871.

[24] W. Kohn & L. J. Sham: Self-consistent equations including exchange and correlation effects, *Phys. Rev.* **140**, (1965), A1133–A1138.

[25] A. R. Leach: *Molecular modelling: Principles and applications*, 2nd ed., Pearson Education, 2001.

[26] S. H. Vosko, L. Wilk, & M. Nusair: Accurate spin-dependent electron liquid correlation energies for local spin density calculations: A critical analysis, *Can. J. Phys.* **58**, (1980), 1200–1211.

[27] D. C. Langreth & M. J. Mehl: Beyond the local-density approximation in calculations of ground-state electronic properties, *Phys. Rev. B* **28**, (1983), 1809–1834.

[28] A. D. Becke: Density-functional exchange-energy approximation with correct asymptotic behavior, *Phys. Rev. A* **38**, (1988), 3098–3100.

[29] J. P. Perdew, M. Ernzerhof, & K. Burke: Rationale for mixing exact exchange with density functional approximations, *J. Chem. Phys.* **105**, (1996), 9982–9985.

[30] A. D. Becke: A new mixing of Hartree–Fock and local density-functional theories, *J. Chem. Phys.* **98**, (1993), 1372–1377.

[31] C. Lee, W. Yang, & R. G. Parr: Development of the Colle-Salvetti correlation-energy formula into a functional of the electron density, *Phys. Rev. B* **37**, (1988), 785–789.

[32] F. Jensen: *Introduction to computational chemistry*, 2nd ed., John Wiley & Sons, 2007.

[33] F. London: Théorie quantique des courants interatomiques dans les combinaisons aromatiques, *J. Phys. Radium* **8**, (1937), 397–409.

[34] K. Wolinski, J. F. Hinton, & P. Pulay: Efficient implementation of the gauge-independent atomic orbital method for NMR chemical shift calculations, *J. Am. Chem. Soc.* **112**, (1990), 8251–8260.

[35] K. A. Peterson, D. Figgen, E. Goll, H. Stoll, & M. Dolg: Systematically convergent basis sets with relativistic pseudopotentials. II. Small-core pseudopotentials and correlation consistent basis sets for the post-*d* group 16–18 elements, *J. Chem. Phys.* **119**, (2003), 11113–11123.

[36] J. Autschbach & S. Zheng: Relativistic computations of NMR parameters from first principles: Theory and applications, *Annu. Rep. NMR Spectrosc.* **67**, (2009), 1–95.

[37] H.-J. Werner, P. J. Knowles, G. Knizia, F. R. Manby, & M. Schütz: Molpro: A general-purpose quantum chemistry program package, *WIREs Comput. Mol. Sci.* **2**, (2012), 242–253.

[38] H.-J. Werner, P. J. Knowles, G. Knizia, F. R. Manby, M. Schütz, P. Celani, *et al.*: *MOLPRO, version 2012.1, a package of ab initio programs*, see `http://www.molpro.net`, Cardiff, UK, 2012.

[39] C. Hampel, K. A. Peterson, & H.-J. Werner: A comparison of the efficiency and accuracy of the quadratic configuration interaction (QCISD), coupled cluster (CCSD), and Brueckner coupled cluster (BCCD) methods, *Chem. Phys. Lett.* **190**, (1992), 1–12.

[40] M. J. Deegan & P. J. Knowles: Perturbative corrections to account for triple excitations in closed and open shell coupled cluster theories, *Chem. Phys. Lett.* **227**, (1994), 321–326.

[41] Th. H. Dunning, Jr.: Gaussian basis sets for use in correlated molecular calculations. I. The atoms boron through neon and hydrogen, *J. Chem. Phys.* **90**, (1989), 1007–1023.

[42] P. Slavíček, R. Kalus, P. Paška, I. Odvárková, P. Hobza, & A. Malijevský: State-of-the-art correlated ab initio potential energy curves for heavy rare gas dimers: Ar_2, Kr_2, and Xe_2, *J. Chem. Phys.* **119**, (2003), 2102–2119.

[43] M. Hanni, P. Lantto, N. Runeberg, J. Jokisaari, & J. Vaara: Calculation of binary magnetic properties and potential energy curve in xenon dimer: Second virial coefficient of ^{129}Xe nuclear shielding, *J. Chem. Phys.* **121**, (2004), 5908–5919.

[44] M. J. Frisch, G. W. Trucks, H. B. Schlegel, G. E. Scuseria, M. A. Robb, J. R. Cheeseman, *et al.*: *Gaussian 09 Revision D.01*, Gaussian Inc. Wallingford CT 2009.

[45] A. Kumar & W. J. Meath: Integrated dipole oscillator strengths and dipole properties for Ne, Ar, Kr, Xe, HF, HCl, and HBr, *Can. J. Chem.* **63**, (1985), 1616–1630.

[46] P. Ren & J. W. Ponder: Consistent treatment of inter- and intramolecular polarization in molecular mechanics calculations, *J. Comput. Chem.* **23**, (2002), 1497–1506.

[47] G. Bussi, T. Zykova-Timan, & M. Parrinello: Isothermal-isobaric molecular dynamics using stochastic velocity rescaling, *J. Chem. Phys.* **130**, (2009), 074101.

[48] G. J. Martyna, M. E. Tuckerman, D. J. Tobias, & M. L. Klein: Explicit reversible integrators for extended systems dynamics, *Mol. Phys.* **87**, (1996), 1117–1157.

[49] TURBOMOLE V6.5 2013, a development of University of Karlsruhe and Forschungszentrum Karlsruhe GmbH, 1989-2007, TURBOMOLE GmbH, since 2007; available from http://www.turbomole.com.

[50] C. Angeli, K. L. Bak, V. Bakken, O. Christiansen, R. Cimiraglia, S. Coriani, *et al.*: *Dalton2011, a molecular electronic structure program (2011), see* http://www.daltonprogram.org.

[51] K. Eichkorn, F. Weigend, O. Treutler, & R. Ahlrichs: Auxiliary basis sets for main row atoms and transition metals and their use to approximate Coulomb potentials, *Theor. Chem. Acc.* **97**, (1997), 119–124.

[52] J. Vaara, M. Hanni, & J. Jokisaari: Nuclear spin-spin coupling in a van der Waals-bonded system: Xenon dimer, *J. Chem. Phys.* **138**, (2013), 104313.

[53] J. Roukala, J. Zhu, C. Giri, K. Rissanen, P. Lantto, & V.-V. Telkki: Encapsulation of xenon by a self-assembled Fe_4L_6 metallosupramolecular cage, *J. Am. Chem. Soc.* **137**, (2015), 2464–2467.

[54] M. Hanni, P. Lantto, M. Repiský, J. Mareš, B. Saam, & J. Vaara: Electron and nuclear spin polarization in Rb-Xe spin-exchange optical hyperpolarization, *Phys. Rev. A* **95**, (2017), 032509.

[55] E. van Lenthe, E. J. Baerends, & J. G. Snijders: Relativistic regular two-component Hamiltonians, *J. Chem. Phys.* **99**, (1993), 4597–4610.

[56] E. van Lenthe, E. J. Baerends, & J. G. Snijders: Relativistic total energy using regular approximations, *J. Chem. Phys.* **101**, (1994), 9783–9792.

[57] S. K. Wolff & T. Ziegler: Calculation of DFT-GIAO NMR shifts with the inclusion of spin-orbit coupling, *J. Chem. Phys.* **109**, (1998), 895–905.

[58] S. K. Wolff, T. Ziegler, E. VAN Lenthe, & E. J. Baerends: Density functional calculations of nuclear magnetic shieldings using the zeroth-order regular approximation (ZORA) for relativistic effects: ZORA nuclear magnetic resonance, *J. Chem. Phys.* **110**, (1999), 7689–7698.

[59] G. te Velde, F. M. Bickelhaupt, E. J. Baerends, C. Fonseca Guerra, S. J. A. van Gisbergen, J. G. Snijders, *et al.*: Chemistry with ADF, *J. Comput. Chem.* **22**, (2001), 931–967.

[60] ADF2016, SCM, Theoretical Chemistry, Vrije Universiteit, Amsterdam, The Netherlands, http://www.scm.com.

[61] G. Schreckenbach & T. Ziegler: Calculation of NMR shielding tensors using gauge-including atomic orbitals and modern density functional theory, *J. Phys. Chem.* **99**, (1995), 606–611.

[62] M. Krykunov, T. Ziegler, & E. van Lenthe: Hybrid density functional calculations of nuclear magnetic shieldings using Slater-type orbitals and the zeroth-order regular approximation, *Int. J. Quantum Chem.* **109**, (2009), 1676–1683.

[63] J. Autschbach: Magnitude of finite-nucleus-size effects in relativistic density functional computations of indirect NMR nuclear spin–spin coupling constants, *ChemPhysChem* **10**, (2009), 2274–2283.

[64] E. van Lenthe & E. J. Baerends: Optimized Slater-type basis sets for the elements 1–118, *J. Comput. Chem.* **24**, (2003), 1142–1156.

[65] W. Humphrey, A. Dalke, & K. Schulten: VMD: Visual molecular dynamics, *J. Mol. Graphics* **14**, (1996), 33–38.

[66] J. Mareš & J. Vaara: Solvation structure and dynamics of Ni^{2+}(aq) from a polarizable force field, *Chem. Phys.* **443**, (2014), 112–122.

[67] J.-P. Piquemal, L. Perera, G. A. Cisneros, P. Ren, L. G. Pedersen, & T. A. Darden: Towards accurate solvation dynamics of divalent cations in water using the polarizable amoeba force field: From energetics to structure, *J. Chem. Phys.* **125**, (2006), 054511.

[68] J. C. Wu, J.-P. Piquemal, R. Chaudret, P. Reinhardt, & P. Ren: Polarizable molecular dynamics simulation of Zn(II) in water using the AMOEBA force field, *J. Chem. Theory Comput.* **6**, (2010), 2059–2070.

[69] D. Semrouni, I. William C. Isley, C. Clavaguéra, J.-P. Dognon, C. J. Cramer, & L. Gagliardi: Ab initio extension of the AMOEBA polarizable force field to Fe^{2+}, *J. Chem. Theory Comput.* **9**, (2013), 3062–3071.

[70] R Friedberg & J. E. Cameron: Test of the Monte Carlo method: Fast simulation of a small Ising lattice, *J. Chem. Phys.* **52**, (1970), 6049–6058.

[71] P. Peuravaara *et al.*, Manuscript in preparation.

[72] M. Hanni, P. Lantto, & J. Vaara: Pairwise additivity in the nuclear magnetic resonance interactions of atomic xenon, *Phys. Chem. Chem. Phys.* **11**, (2009), 2485–2496.

[73] J. Schnitker & A. Geiger: NMR quadrupole relaxation of xenon-131 in water, *Z. Phys. Chem.* **155**, (1987), 29–54.

[74] F. H. Stillinger & A. Rahman: Improved simulation of liquid water by molecular dynamics, *J. Chem. Phys.* **60**, (1974), 1545–1557.

[75] M. Ylihautala, J. Lounila, & J. Jokisaari: Nuclear magnetic shielding of noble gases in liquid crystals, *J. Chem. Phys.* **110**, (1999), 6381–6388.

[76] J. Saunavaara & J. Jokisaari: Determination of sample temperature and temperature stability with ^{129}Xe NMR, *J. Magn. Reson.* **180**, (2006), 58–62.